https://doi.org/10.5194/egusphere-2026-4695
Preprint. Discussion started: 24 August 2026

Seasonal Differences in Correlations and Contributions of Photochemical, Upwind Cloud and Aerosol Aqueous-Phase Oxidation, and Mixed Combustion in Secondary Organic Aerosol Formation in Coastal Southern California

Veronica Z. Berta[1], Lynn M. Russell[1], Abigail S. Williams[1], Jeramy L. Dedrick[1], Sanghee Han[1], Dan Lubin[1], Ryan N. Farley[2], Allison C. Aiken[2], Jeremy Wentzell[3], John Liggio[3]

[1] Scripps Institution of Oceanography, University of California San Diego, La Jolla, CA 92093, USA
[2] Earth and Environmental Sciences Division, Los Alamos National Laboratory, Los Alamos, NM 87545, USA
[3] Air Quality Research Division, Environment and Climate Change Canada, Toronto, ON M3H 5T4, Canada

Correspondence to: Lynn M. Russell (lmrussell@ucsd.edu)

Abstract. Organic aerosol (OA) formation in coastal environments is influenced by photochemical and aqueous-phase oxidation, but their relative contributions remain poorly constrained. During the Eastern Pacific Cloud Aerosol Precipitation Experiment (EPCAPE), Aerosol Mass Spectrometer measurements at Mt. Soledad in La Jolla, California were analyzed by positive matrix factorization to resolve four oxygenated OA (OOA) factors: sulfate-related (SR-OOA), more-oxidized (MO-OOA), less-oxidized (LO-OOA), and continental (C-OOA). SR-OOA was linked to marine biogenic sources and bimodal number distributions indicating in-cloud aqueous reactions. Multiple linear regression (MLR) associated SR-OOA with in-cloud aqueous reactions represented by upwind cloud vertical fraction (UCVF; 70%). MO-OOA correlated with UCVF during months with increasing UCVF (R = 0.25–0.66) and ozone for 11 months (R = 0.36–0.76), indicating both in-cloud aqueous and photochemical oxidation. MLR showed contributions from in-cloud aqueous reactions in spring (48%) and photochemical oxidation represented by ozone in summer, fall, and winter (44–77%) to MO-OOA. LO-OOA showed an ozone correlation (R = 0.37) and midday maxima, while MLR associated LO-OOA with photochemical oxidation (64%). C-OOA correlated with refractory black carbon (rBC; R = 0.33) and other combustion tracers. MLR associated C-OOA with combustion represented by rBC in winter (49%), aerosol water aqueous oxidation represented by relative humidity (RH) in spring (37%), and photochemical oxidation in summer and fall (37–43%). O/C was explained by RH (39%) and ozone (38%), followed by UCVF (19%). These results reveal distinct seasonal contributions of photochemical and aqueous-phase oxidation to biogenic and mixed combustion OA in coastal Southern California.

https://doi.org/10.5194/egusphere-2026-4695
Preprint. Discussion started: 24 August 2026

1 Introduction

Organic aerosol (OA) is a major component of submicron particle mass concentration in coastal and urban environments and is comprised of a complex mixture of compounds with a wide range of properties such as composition, size, and volatility (Hallquist et al., 2009;Jimenez et al., 2009). Secondary organic aerosol (SOA), which represents a large fraction of fine aerosol mass in many regions (Zhang et al., 2007), is formed through atmospheric reactions of volatile and semi-volatile organic compounds with oxidants such as nitrate radicals, ozone, and hydroxyl radicals, leading to the formation of lower-volatility products that partition into the particle phase. Consequently, SOA often reflects contributions from various precursor sources, including biogenic emissions as well as mixed combustion sources with both biomass burning and fossil fuel emissions.

The oxidation state and composition of SOA evolve through a combination of gas-phase oxidation and multiphase reactions. Gas-phase oxidation by photochemically produced oxidants transforms gaseous precursors into lower-volatility products that partition into the particle phase and also contribute to the aging of existing aerosol, generally increasing the oxygen content of organic aerosol (Kroll and Seinfeld, 2008). These processes are closely linked to photochemical activity and downwelling shortwave (DSW) solar radiation. In addition to gas-phase oxidation, aqueous-phase reactions within cloud droplets and aerosol liquid water provide an alternative pathway for SOA formation and aging (Ervens et al., 2011;Carlton and Turpin, 2013). Multiphase reactions occurring in cloud droplets and in aerosol liquid water under high relative humidity can produce highly oxidized organic components through aqueous reactions involving dissolved organic compounds and inorganic oxidants (Carlton et al., 2020;McNeill, 2015). However, disentangling the relative contributions of photochemical oxidation, aerosol water aqueous reactions, and in-cloud aqueous reactions remains challenging because these processes often occur simultaneously and respond to co-varying meteorological conditions.

Previous studies have shown that SOA formation pathways differ across oxygenated organic aerosol (OOA) components and environmental conditions (Table S1). Photochemical oxidation is often associated with the formation of less-oxidized OOA (LO-OOA), while more-oxidized OOA (MO-OOA) reflects contributions from both photochemical aging and aqueous-phase reactions. For example, Xu et al. (2017) and Xiao et al. (2021) found that LO-OOA was strongly associated with odd oxygen ($O_X = O_3 + NO_2$) in relatively polluted Beijing, China, whereas MO-OOA increased with relative humidity (RH) and aerosol liquid water content (ALWC) calculated from relative humidity, temperature, and aerosol composition, which was interpreted as reflecting a transition from photochemical to multiphase reactions during aerosol evolution. Consistent with this, Huang et al. (2020) showed that the oxidation state of OA was more strongly associated with photochemical oxidants than with ALWC, while SOA mass concentrations could be more strongly influenced by aqueous-phase reactions under conditions of elevated ALWC and aqueous precursor availability. Diurnal trends in MO-OOA mass concentrations and ALWC indicated that MO-OOA is formed through aqueous-phase reactions (Yao et al., 2022), and that aqueous reactions can contribute more strongly

https://doi.org/10.5194/egusphere-2026-4695
Preprint. Discussion started: 24 August 2026

to MO-OOA than to LO-OOA even when SOA formation is largely associated with photochemical oxidation (Li et al., 2021). Using combined indicators of ALWC and photochemical oxidants, Zhan et al. (2021) further demonstrated that LO-OOA and MO-OOA can reflect distinct but overlapping contributions from aqueous and photochemical pathways, with aqueous reactions becoming more important under low-oxidant conditions. Together, these studies indicate that the formation and evolution of SOA components reflect a combination of photochemical and multiphase reactions, with their relative contributions varying across environmental conditions. Previous studies have largely relied on qualitative relationships between SOA components and environmental variables such as RH, ALWC, and photochemical oxidants, often identifying when photochemical or aqueous reactions are dominant but not quantitatively separating the individual contributions of these pathways across different OOA factors, with few relevant to coastal environments.

Clouds and high relative humidity play a central role in modulating the balance between photochemical oxidation and aqueous-phase SOA formation. Overlying cloud layers attenuate actinic flux below cloud base, reducing photolysis rates and suppressing photochemical activity within the boundary layer (Imanova et al., 2025;Barth et al., 2002;Hall et al., 2018). At the same time, clouds and high relative humidity drive aqueous-phase reactions by increasing the availability of liquid water. An increase in cloud droplet liquid water content (LWC) has previously been found to be associated with increases in both MO-OOA and LO-OOA mass concentrations in interstitial aerosols as well as an increase of 0.1–0.15 in the oxygen-to-carbon ratio (O/C), representing the oxidation of organic components, for SOA (Gao et al., 2025). As a result, cloud influence can either suppress or amplify organic aerosol oxidation depending on the balance between reduced photochemical activity and enhanced aqueous reactions. While previous studies have linked cloud and high-RH conditions to greater SOA oxidation (Lim et al., 2010), the extent to which cloud aqueous reactions affect distinct OOA factors during regional transport, including the influence of upwind cloud aqueous reactions in increasing the amount of oxidized organic components prior to arrival at a coastal receptor site, remains poorly understood.

Southern California, and in particular the coastal region near La Jolla, provides an ideal setting to investigate these processes. This region is frequently influenced by a persistent marine boundary layer characterized by stratocumulus cloud cover, climatologically-consistent back-trajectories, high relative humidity, strong gradients in solar radiation, and organic components making up the largest fraction (48%) of submicron mass (Han et al., 2025). At the same time, it is impacted by anthropogenic emissions and aged air masses transported from the Los Angeles Basin and surrounding urban areas (Ault et al., 2009;Hawkins and Russell, 2010;Liu et al., 2011;Day et al., 2010). These conditions create a dynamic environment in which both photochemical and aqueous reactions may contribute to SOA formation, yet the relative importance of photochemical production, aerosol water reactions, and regional in-cloud aqueous reactions has not been quantitatively assessed.

https://doi.org/10.5194/egusphere-2026-4695
Preprint. Discussion started: 24 August 2026

This study uses High-Resolution Time-of-Flight Aerosol Mass Spectrometer (HR-ToF-AMS) measurements to characterize the composition and variability of non-refractory submicron aerosol at a coastal site in Southern California for almost 12 months. The overall trends in the inorganic and organic components and their semivolatile partitioning between two nearby sites have already been quantified (Han et al., 2025), but here we examine changes in organic composition associated with the degree of oxidation and source types using real-time measurements. In addition, we evaluate similarities in seasonal and diurnal patterns and across air masses between organic aerosol components and oxidation tracers (namely ozone, relative humidity, upwind cloud vertical fraction, and local cloud fraction) as well as a mixed combustion tracer (refractory black carbon, rBC) to distinguish between sources of photochemical reactions, cloud water and aerosol water aqueous reactions, and primary emissions. To assess the relative contributions of these processes to variability, we use multivariate linear regression (MLR) to provide a combined assessment of different processes. Together, these results provide insight into the relative importance of photochemical and multiphase pathways in governing organic aerosol oxidation in a coastal marine environment.

2 Methods

The Eastern Pacific Cloud Aerosol Precipitation Experiment (EPCAPE) took place from 15 February 2023 to 14 February 2024 in La Jolla, California, and included two sites located approximately 3 km apart: Scripps Pier (32.87° N, 117.26° W; 7 m ASL) and Mt. Soledad (32.84° N, 117.25° W; 251 m ASL) (Russell et al., 2023). Aerosol and gas measurements herein exclude particle concentrations exceeding 8,000 cm^{-3} to account for short-lived contamination events (Han et al., 2025). At Mt. Soledad, out of cloud measurements were sampled using an isokinetic, wind-facing inlet when visibility was above 5 km. Cloud droplet residuals were sampled while in cloud when visibility was below 5 km using a Counterflow Virtual Impactor (CVI; Brechtel Manufacturing Inc., Hayward, CA) but were excluded from this analysis. Pearson correlation coefficients (R) in this work are described as weak ($0.25 \leq R < 0.50$), moderate ($0.50 \leq R < 0.80$), and strong ($0.80 \leq R$) (Devore et al., 2012). A threshold of $p < 0.05$ is used to determine statistical significance.

2.1 Online Aerosol and Gas Composition Measurements

Submicron non-refractory (NR) organic (Org), nitrate (NO_3^-), sulfate (SO_4^{2-}), ammonium (NH_4^+), and chloride (Chl^-) mass was measured every 5 minutes by a High Resolution Time-of-Flight Aerosol Mass Spectrometer (HR-ToF-AMS; Aerodyne Research Inc., Billerica, MA) at Mt. Soledad (Han et al., 2025). Mass concentrations were corrected using a monthly collection efficiency (CE) ranging from 0.4 to 0.9. The CE was determined for each instrument by comparing mass concentrations from particle size distributions while accounting for refractory components including black carbon, dust, and sea salt (Berta et al., 2025).

https://doi.org/10.5194/egusphere-2026-4695
Preprint. Discussion started: 24 August 2026

The HR-ToF-AMS cycled periodically every 5 minutes between different ion flight modes which included a 2-minute, size-resolved, high sensitivity, V mode. V mode measurements were analyzed by the data analysis software packages SQUIRREL (SeQUential Igor data RetRiEvaL), version 1.64, for pre-processing and PIKA (Peak Integration by Key Analysis), version 1.24, on Igor Pro 8 (WaveMetrics, Inc.) for high-resolution analysis of individual ion fragments. Measurements of single particle composition from the event-trigger mode (2 minutes of each cycle) are also available (Berta et al., 2025) and are investigated in other work (Williams et al., in review).

A single-particle soot photometer (SP2; Droplet Measurement Technologies) provided 1-minute refractory black carbon (rBC) measurements (Berta et al., 2025), and a UV photometer-based ozone (O_3) analyzer (Model 49C, Thermo Environmental Instruments) provided 1-second ambient ozone concentration. From April 30 2023 to June 6 2023, a high resolution time-of-flight chemical ionization mass spectrometer (HR-ToF-CIMS) operated with iodide (I-) ionization measured trace organic gases (Liggio et al., 2025). Twenty-seven organic acids were calibrated and quantified, while isocyanic acid (HNCO) was evaluated using measured ion signal intensity due to the absence of a calibration standard. A Scanning Electrical Mobility Spectrometer (SEMS; 10-900 nm mobility diameter, BMI) and Aerodynamic Particle Sizers (APS; 0.5-20 µm aerodynamic diameter, TSI) provided ambient (out-of-cloud) aerosol size distributions. SEMS and APS distributions were merged following Saliba et al. (2019) to span a range of 0.01-10 µm (Berta et al., 2025;Dedrick et al., 2026). Particle number concentrations were measured at 1-second resolution using a condensation particle counter (CPC; Model 3010, TSI).

2.2 Offline Filter Measurements

Aerosol filter samples were collected at Mt. Soledad for offline analysis of non-volatile (NV) organic functional groups and elemental composition for three size cuts. Particles were sampled for 23 hours (7 PM to 6 PM PT) either behind a <1 µm cyclone or downstream of <0.18 µm and <0.5 µm Berner impactors. Samples were collected on pre-scanned 37 mm Teflon filters (Pall Inc., 1.0 µm pore size) and stored at 0°C prior to analysis. Filters were equilibrated to room temperature before analysis by Fourier Transform Infrared Spectroscopy (FTIR; Bruker Optics, Tensor 27 spectrometer). The FTIR spectrum was fitted with peaks corresponding to alcohol, alkane, amine, carboxylic acid, and non-acid carbonyl functional groups to quantify their mass concentrations (Takahama et al., 2013;Pelayo et al., 2025). Positive Matrix Factorization (PMF) was applied to <1 µm size cut FTIR spectra to identify organic aerosol factors across samples. The FTIR 4-factor PMF solution identifies sulfate-correlated emissions (SC), fossil fuel combustion emissions (FF), dust-correlated emissions (DC), and biomass burning emissions (BB) based on correlations with chemical tracers, characteristic functional group composition, and spectral similarity to previously identified PMF factors (Pelayo et al., 2025).

A subset of submicron filters at Mt. Soledad and at Scripps Pier was analyzed by Chester Labnet (Tigard, OR, USA) using X-ray fluorescence (XRF). XRF analysis provided concentrations for elements ranging from Na to Ba (Maria et al., 2003). Sea

https://doi.org/10.5194/egusphere-2026-4695
Preprint. Discussion started: 24 August 2026

salt mass concentrations were calculated as Na (μg m^{-3}) × 1.47 + Cl (μg m^{-3}) (Berta et al., 2023;Saliba et al., 2020;Frossard et al., 2014;Bates et al., 2012;Quinn et al., 2019). Dust mass concentrations were calculated from elemental concentrations assuming mineral oxides of $MgCO_3$, Al_2O_3, SiO_2, K_2O, $CaCO_3$, TiO_2, Fe_2O_3, MnO, and BaO after excluding the contribution from sea salt (Usher et al., 2003). Non-sea-salt potassium (nssK) was calculated as K (μg m^{-3}) - Na (μg m^{-3}) × (ratio of K to Na in seawater) (Berta et al., 2023). Sea salt, dust, and nssK mass concentrations reported here were averaged by the week (Berta et al., 2025).

2.3 PMF Analysis of AMS NR Organic Mass

Positive matrix factorization of ambient and CVI measurements of high resolution (HR) organic AMS data was performed using the PMF Evaluation Tool, PET (Ulbrich et al., 2009). Ion fragments with low signal-to-noise (SNR) were downweighted ($0.2 < SNR < 2$) by a factor of 2 or removed ($SNR < 0.2$). Ion fragments associated with m/z 44 (CO_2^+, CO^+, H_2O^+, HO^+, O^+) were also downweighted by a factor of 2. No data smoothing or spike removal was applied to the matrices.

Fit quality (Q/Q_{exp}) and uncentered correlations were used to identify the best number of factors. Q/Q_{exp} decreases with an increasing number of factors as each factor introduces an additional degree of freedom. Solutions with numbers of factors that resolve Q/Q_{exp} near a value of 1 are ideal such that an increased distance of Q/Q_{exp} from 1 is used as one of the criteria for rejecting a solution. The 1 to 8 factor solutions and criteria of PMF analysis are summarized in Table S2. The "OminusC" data type, obtained by subtracting the "Open" ion sticks from the "Closed" ion sticks after peak fitting, was used for PMF analysis. The final number of factors selected was the highest number for which temporal correlations (R) between factor pairs were below 0.8, adding an additional factor did not reduce the absolute residual or result in a factor that contributed less than 10% of the mass. Therefore, a 5-factor solution with a Q/Q_{exp} value of 1.83 was obtained for the campaign.

2.4 Back-Trajectory Analysis

Source regions of air masses were identified every 3 hours using k-means clustering of 48-hour back-trajectories calculated using the Hybrid Single-Particle Lagrangian Integrated Trajectory (HYSPLIT) model (Silber et al., 2025). The clustering analysis grouped the trajectories into five representative air mass classes during the campaign (Han et al., 2025;Maneenoi et al., 2025). These classes correspond to coastal northwesterly air masses following the California coastline (CNW), air masses from the Los Angeles and Long Beach region (LALB), southerly air masses from near Tijuana, Mexico (SOU), continental easterly air masses from inland Southern California (EAS), and marine westerly air masses transported over the Pacific Ocean (MWE).

https://doi.org/10.5194/egusphere-2026-4695
Preprint. Discussion started: 24 August 2026

2.5 Meteorological and Cloud-Related Measurements

Downwelling shortwave radiation (DSW; 280–2800 nm) was measured using Eppley Precision Spectral Pyranometers (PSP) (Jayaraman et al., 1998;Lubin and Simpson, 1997). Periods of missing data at Mt. Soledad were supplemented with SKYRAD measurements from the ARM site at Scripps Pier (Sengupta et al., 2023). Meteorological parameters, including ambient temperature, wind speed, wind direction, precipitation, and relative humidity (RH), were measured using a Vaisala Weather Transmitter at Mt. Soledad. Upwind cloudiness was quantified using the Upwind Cloud Vertical Fraction (UCVF), derived from Scripps Pier back-trajectories combined with SatCORPS satellite retrievals of low-cloud (0-2000 m) top and base heights, representing the fraction of the planetary boundary layer influenced by clouds over the preceding 24 hours (Berta et al., 2025;Maneenoi et al., 2025). 30-minute SatCORPS/GOES satellite cloud fraction (SCF) retrievals were used to characterize regional cloudiness. SCF was calculated as the ratio of cloudy pixels to total pixels within a 0.2° × 0.2° bounding box centered at Kearny Mesa, California (32.8250° N, 117.1392° W), corresponding to approximately 100 pixels at the native 0.02° × 0.02° SatCORPS spatial resolution. A second SCF dataset was generated by shifting the bounding box 0.4° westward to better capture marine/coastal cloud conditions near Mt. Soledad while minimizing overlap between the two regions. A ground-based Total Sky Imager (Yankee Environmental Systems, Inc.) was used to obtain local cloud fraction (LCF) as the sum of opaque and thin cloud fractions. Local sea surface temperature (SST) was obtained from the Southern California Coastal Ocean Observing System (SCCOOS) automated shore station at Scripps Pier (Carter et al., 2022).

2.6 Multiple Linear Regression

Multiple Linear Regression (MLR) was used to identify the dependence of organic oxidation and SOA mass concentrations on numerous primary and secondary processes variables (X_p). Since the chosen variables were not normally distributed, each observation of the predictor variables (X_i) was normalized using min-max normalization prior to regression:

$$X_{i,norm} = \frac{X_i - \min(X)}{max(X) - min(X)} \quad (1)$$

MLR models were then fit using the fitlm() function from MATLAB:

$$Y = b + m_1X_1 + m_2X_2 + \cdots + m_pX_p \quad (2)$$

where b is the intercept and is set to the origin, m_p are the regression coefficients corresponding to the predictor variables X_p, and Y represents the model-predicted value. The relative contribution from each component is represented as the product of the mean normalized predictor value (X_p) and the magnitude of its regression coefficient (m_p), divided by the sum of the magnitudes of the intercept (b) and all m_pX_p predictor terms.

https://doi.org/10.5194/egusphere-2026-4695
Preprint. Discussion started: 24 August 2026

3 Results

To characterize AMS NR organic aerosol sources, PMF was applied to the AMS NR organic mass spectra, excluding the inorganic fragments. The covariability of the resulting NR organic factors and tracers related to mixed combustion and oxidation is assessed through seasonal and diurnal cycles and for different air mass source regions.

3.1 Sources of NR Organic Aerosols at Mt. Soledad

The five-factor PMF solution at Mt. Soledad included a hydrocarbon-like organic aerosol (HOA) factor and four oxygenated organic aerosol (OOA) factors: sulfate-related OOA (SR-OOA) factor, more-oxidized OOA (MO-OOA) factor, less-oxidized OOA (LO-OOA) factor, and a continental OOA (C-OOA) factor. PMF factors were previously reported for a combined analysis with both organic and inorganic fragments for October-December for measurements from the Los Alamos National Laboratory (LANL) HR-ToF-AMS at Mt. Soledad (Farley et al., 2026). Here PMF used only organic fragments and included the full year of Scripps Institution of Oceanography (SIO) HR-ToF-AMS measurements at Mt. Soledad. By excluding inorganic fragments, the year-long analysis resolved a factor characterized by methanesulfonic acid (MSA)-related peaks, which was likely obscured by the stronger inorganic signals in the year-long analysis. Otherwise, the 12-month organic-only PMF solution showed good agreement with the 2-month PMF solution including both organic and inorganic fragments reported by Farley et al. (2026): The MO-OOA factors (R = 0.91), C-OOA factors (R = 0.84) and HOA factors (R = 0.91) all strongly correlated with each other. The organic-only SR-OOA factor correlated most strongly with the OOA factor containing inorganic sulfate (sulfate-OOA; R = 0.59) and marine-derived nitrogen organic aerosol (NOA; R = 0.62) factors. Comparisons to organic-only PMF factors from the Aerosol Chemical Speciation Monitor (ACSM) at Scripps Pier during EPCAPE show that the strongest correlations were the MSA factor with SR-OOA (R = 0.34), less-volatile (LV)-OOA with MO-OOA (R = 0.81) and LO-OOA (R = 0.67), semi-volatile (SV)-OOA with C-OOA (R = 0.62), and HOA with HOA (R = 0.52) (Zawadowicz et al., 2023). The mass spectra, annual time series with 5-minute resolution, and monthly-averaged mass fraction of each factor are available in Fig. S1–S3; Table S3 shows the average and median mass concentrations and organic elemental ratios. The most abundant PMF factor was MO-OOA which comprised 32 ± 19% of ambient NR organic mass (and has an average ambient concentration of 0.78 ± 1.36 μg m^{-3}). This factor was followed by C-OOA at 25 ± 20% (0.63 ± 0.90 μg m^{-3}), SR-OOA at 16 ± 17% (0.18 ± 0.21 μg m^{-3}), LO-OOA at 14 ± 18% (0.24 ± 0.45 μg m^{-3}), and HOA at 14 ± 15% (0.21 ± 0.34 μg m^{-3}).

The SR-OOA factor has the highest sulfur-to-carbon ratio (S/C; 1.1 × 10^{-2}) and the second highest O/C (1.00) among all factors (Table S3). Its mass spectrum showed unique peaks at m/z 45 (CHS^+), m/z 47 (CH_3S^+), m/z 78 ($CH_2SO_2^+$), m/z 79 ($CH_3SO_2^+$), and m/z 96 ($CH_4SO_3^+$) that contributed to the elevated S/C and are attributed to MSA (Crippa et al., 2013;Huang et al., 2017;Nojgaard et al., 2022;Song et al., 2024;Zorn et al., 2008). MSA is formed from the oxidation of dimethylsulfide (DMS),

https://doi.org/10.5194/egusphere-2026-4695
Preprint. Discussion started: 24 August 2026

a product of phytoplankton decomposition, indicating a marine biogenic contribution to this factor. In addition, SR-OOA shows weak to moderate correlations to relative humidity (R = 0.33, Table S4) and upwind cloud vertical fraction (UCVF; R = 0.52, Table S4), supporting secondary aerosol formation through aqueous-phase reactions. Consistent with this interpretation, SR-OOA is strongly correlated to AMS NR sulfate (R = 0.84, Table S4), which is secondary in formation. ACSM NR sulfate measured at Scripps Pier was previously shown to be largely from marine biogenic sources during EPCAPE based on its correlation with local SST as an indicator of phytoplankton activity (Maneenoi et al., 2025). Of the five organic PMF factors, SR-OOA also exhibited the strongest correlation with local SST (R = 0.43, Table S4), consistent with both sulfate and MSA being largely driven by marine biogenic sources (Maneenoi et al., 2025). Ultrafine measurements of MSA from a Thermal Desorption Chemical Ionization Mass Spectrometer (TD-CIMS) did not correlate with SR-OOA or any other factor, likely reflecting differences in the particle size ranges sampled by the TD-CIMS and HR-ToF-AMS (Kapp and Smith, 2025). SR-OOA is negatively correlated to dust (R = -0.27, Table S4), a submicron FTIR NV organic PMF factor correlated to dust (R = -0.34, Table S5), and particle number concentration (R = -0.30, Table S4). These negative correlations likely reflect contrasting source regions, with dust and related NV organic components primarily originating from the Salton Sea to the north and east of the La Jolla sites (Han et al., 2025), whereas SR-OOA is consistent with marine sources associated with cleaner air masses from over the Pacific Ocean to the west and northwest.

The MO-OOA factor had the highest O/C at 1.47. This factor is characterized by prominent peaks at m/z 28 (CO^+) and m/z 44 (CO_2^+), which are fragments from the decomposition of carboxylic acids and their derivatives, indicating that this factor is likely strongly linked to secondary organic aerosol formation (Duplissy et al., 2011). A high ratio of m/z 44 to m/z 43, also indicative of highly oxidized aerosol, is used to identify this factor as well as comparisons to previously reported less-volatile LV-OOA and MO-OOA factors (Crippa et al., 2013;Hu et al., 2013;Ng et al., 2010; Hayes et al., 2013). Likewise, MO-OOA is weakly correlated to secondary AMS NR components including sulfate (R = 0.43, Table S4) and nitrate (R = 0.33, Table S4). Submicron FTIR NV acid groups had the strongest correlations to SR-OOA (R = 0.64, Table S5) and MO-OOA (R = 0.55, Table S5), consistent with these factors having the highest O/C ratios. Correlations between FTIR NV acid groups and these AMS NR PMF organic factors were weaker for smaller particle sizes (Table S5), consistent with previous observations that stronger correlations occur when these functional groups are associated with larger particles, where they contribute a larger fraction of the submicron aerosol mass (Berta et al., 2023).

The LO-OOA factor is characterized by lower contributions from m/z 28 and 44 to its mass spectrum than to MO-OOA. Compared to MO-OOA which had a m/z 44 to m/z 43 ratio of ~14, the ratio of m/z 44 to m/z 43 for LO-OOA is ~2 , LO-OOA likely has an anthropogenic source that is subsequently formed by oxidation due to weak correlations to particle number concentration measured by the CPC (R = 0.36), AMS NR chloride (R = 0.25), and ozone (R = 0.37) and a moderate correlation with AMS NR nitrate (R = 0.52), as seen in Table S4.

https://doi.org/10.5194/egusphere-2026-4695
Preprint. Discussion started: 24 August 2026

The mass spectrum of C-OOA contained unique peaks at m/z 27 (CHN^+), m/z 41 ($C_2H_2N^+$), and m/z 43 ($CHNO^+$), contributing the highest nitrogen-to-carbon ratio (N/C; 1.3×10^{-2}, Table S3) of the factors. C-OOA also contained a large signal at m/z 29 which is attributed primarily to CHO^+ rather than unoxygenated $C_2H_5^+$, as observed for the LO-OOA factor. Similarly, signals at m/z 43 and 57 were attributed to oxygenated fragments ($C_2H_3O^+$ and $C_3H_5O^+$) rather than hydrocarbon fragments ($C_3H_7^+$ and $C_4H_9^+$), indicating a higher degree of oxidation. These fragmentation patterns are characteristic of biomass burning organic aerosol (He et al., 2010;James et al., 2024). Consistent with this interpretation, C-OOA shows the strongest correlations to biomass burning tracers, including bromine (R = 0.79, Table S4) and non-sea-salt potassium (nss-K; R = 0.55, Table S4) measured by X-Ray Fluorescence (XRF), refractory black carbon (rBC; R = 0.33, Table S4) measured by a Single Particle Soot Photometer (SP2), and a biomass burning (BB) organic PMF factor measured by FTIR (R = 0.71, Table S5). Together, these features indicate that C-OOA is associated with biomass burning emissions and likely represents an oxidized biomass burning organic aerosol component.

The mass spectrum of the HOA factor was characterized by high signal for the ion series $C_nH^+_{2n+1}$ (m/z 29, 43, 57, 71, ...) and $C_nH^+_{2n-1}$ (m/z 41, 55, 69, ...), which are attributed to alkenes, saturated alkanes, and cycloalkanes (Mohr et al., 2012), resulting in the highest hydrogen-to-carbon ratio (H/C; 1.79, Table S3) among all factors. These fragmentation patterns are characteristic of hydrocarbon-like organic aerosol originating from fossil fuel combustion sources such as vehicle emissions. Consistent with a vehicle emission source, HOA was weakly correlated with rBC (R = 0.28, Table S4). The weak correlation likely reflects differences in emission rates of HOA and rBC that depend on fuel type and driving conditions, such as braking associated with the hilltop sampling location (Han et al., 2025) or the presence of lubricating oil that only contributes to the organic mass and not rBC (Sonntag et al., 2012). Among all factors, HOA showed the strongest correlation with particle number concentration measured by the CPC (R = 0.49, Table S4), consistent with its association with primary ultrafine particle emissions. The m/z 55 to 57 ratio is slightly greater than 1 at 1.31, which suggests some contribution from cooking activities (Mohr et al., 2012). Minor signals at m/z 60 ($C_2H_4O_2^+$) and 73 ($C_3H_5O_2^+$), commonly attributed to wood-burning, could indicate a small contribution from cooking as well (He et al., 2010), indicating that both cooking and fresh biomass burning could be influencing this factor. The comparatively smaller signal of these fragments observed for C-OOA is likely due to their reduction during atmospheric aging (Tiitta et al., 2016;Cubison et al., 2011;Alfarra et al., 2007). Additionally, HOA was moderately correlated with FTIR NV alkane functional group mass concentration, with stronger correlations observed in smaller particle sizes (<0.5 µm, R = 0.51; <0.18 µm, R = 0.52, Table S5) compared to submicron particles (R = 0.27, Table S5), supporting the expectation that HOA mass is concentrated in smaller particles characteristic of traffic-related emissions. Similarly, HOA had stronger correlations with FTIR NV organic mass concentration at smaller particle sizes (<0.5 µm, R = 0.51; <0.18 µm, R = 0.54, Table S5) than submicron particles (R = 0.39, Table S5). Despite its hydrocarbon-like composition, HOA had an O/C of 0.32 (Table S3).

https://doi.org/10.5194/egusphere-2026-4695
Preprint. Discussion started: 24 August 2026

3.2 Seasonal and Diurnal Differences in NR Organic Mass

The magnitude of the standard deviation of each organic PMF factor mass concentration exceeds the magnitude of its mean (Table S3), reflecting substantial variability during EPCAPE. As expected, distinct seasonal and diurnal patterns are observed in the PMF factors (Fig. 1–2). Comparison with the seasonal and annual diurnal behavior of tracers of mixed combustion (rBC) and oxidation (O_3, DSW, UCVF, LCF, RH) (Fig. 3–4) allows for assessment of covariability between these variables. Seasonal diurnal variations of these tracers for each season can be found in Figure S4. Monthly correlations of AMS NR PMF factors to mixed combustion and oxidation tracers are available in Table S6.

Similar to previous observations of NR sulfate during EPCAPE (Han et al., 2025;Maneenoi et al., 2025), SR-OOA mass concentrations show a pronounced summertime maximum, peaking at 0.61 ± 0.28 μg m^{-3} in July (Fig. 1a). This peak coincided with increased RH, UCVF, DSW, and LCF (Fig. 3), consistent with greater SOA formation under more photochemically and cloud-influenced conditions. However, among these variables, only UCVF showed a significant correlation with SR-OOA during July (R = 0.48, Table S6), highlighting the importance of regional (upwind) cloud aqueous reactions relative to local cloud conditions. Compared to other oxidized organic factors which correlated with statistical significance to UCVF for up to 4 months, SR-OOA had positive statistically-significant correlations with UCVF for 6 months of the year (Fig. S5, Table S6), supporting its larger contributions from cloud water aqueous-phase reactions. Bimodal number size distributions from merged SEMS and APS measurements, which are more frequent during summer (Dedrick et al., 2026), are associated with elevated SR-OOA concentrations (Fig. 1b), suggesting that the aqueous-phase reactions that contributed to SR-OOA formation also contributed to particle growth in forming the "Hoppel gap" as a result of cloud processing (Hoppel et al., 1990). Similar observations of SOA formation from cloud aqueous reactions have been reported in other marine locations including the Arctic, Atlantic, and Pacific Ocean (Heutte et al., 2025;Dobracki et al., 2025;Xu et al., 2024). In contrast, SR-OOA concentrations were lowest during fall (October–December; 0.05 ± 0.09 μg m^{-3}, Table S7) and winter (January–March; 0.06 ± 0.07 μg m^{-3}, Table S7), when these oxidative tracers (and biogenic source strengths) were also low. The diurnal cycle of SR-OOA showed an evening maximum (Fig. 2a–e), consistent with daytime sea-breezes that brought marine-influenced air masses inland (Han et al., 2025).

Similar to SR-OOA, MO-OOA is also associated with bimodal size distributions (Fig. 1d) and correlates with UCVF, but for 4 months of the year rather than 6 for SR-OOA (Fig. S6, Table S6). These associations are consistent with an SOA component formed by cloud aqueous reactions. MO-OOA increased gradually from spring (April–June; 0.26 ± 0.23 μg m^{-3}, Table S7) into summer (July–September; 1.77 ± 2.08 μg m^{-3}, Table S7), reaching a maximum during late summer in September (2.80 ± 2.83 μg m^{-3}, Fig. 1c). Notably, this increase occurs during the same season in which RH is highest (76 ± 8.6%, Table S7) and ozone is lowest (31.4 ± 7.3 ppb, Table S7). However, ozone increased from its annual minimum in August (29 ± 7 ppb) to September (34 ± 7 ppb), coinciding with the largest month-to-month increase in MO-OOA. In contrast, the other oxidation

https://doi.org/10.5194/egusphere-2026-4695
Preprint. Discussion started: 24 August 2026

tracers (RH, UCVF, DSW, and LCF) remained relatively unchanged or decreased over these months (Fig. 3), suggesting a role of photochemical reactions in MO-OOA formation. Moreover, the peak in MO-OOA mass concentration in September (Fig. 1c) is likely associated with wildfire influence from September 21 to 28 (Aldworth et al., 2024), as reflected by the large difference between the mean (2.80 μg m^{-3}) and median (1.69 μg m^{-3}) mass concentrations. Removing this event reduces the September mean to 1.59 μg m^{-3} and median to 1.51 μg m^{-3}, only slightly higher than the corresponding mean mass concentration of 1.51 μg m^{-3} and median mass concentration of 1.09 μg m^{-3} in August.

On the daily time scale, MO-OOA showed the smallest normalized difference between the maximum and minimum hourly mean concentration among all PMF factors throughout the year (31–65%, Table S7), indicating a comparatively weak diurnal cycle overall (Fig. 1c). The most distinct diurnal patterns occurred during winter (65%) and spring (52%), when MO-OOA concentrations were lowest and the influence of long-range transport was likely reduced, allowing local and boundary layer processes to become more apparent. In contrast, during summer, when MO-OOA concentrations were highest, the normalized difference between the maximum and minimum hourly mean concentration decreased to 31%, consistent with a larger contribution from regionally transported and more uniformly mixed aerosol (Qin et al., 2016;Huang et al., 2020). The organic and inorganic components had very low diurnal variability across seasons due to the daily land-sea breeze transitions characteristic of the coastal environment as well as frequent daytime cloudiness reducing the role of photochemically driven changes (Han et al., 2025). However, during winter and spring, the diurnal cycle of MO-OOA resembled that of ozone with a weak midday increase (13:00–16:00 PT, Fig. 2g,h and S6). The weakness of this correspondence between the MO-OOA component of organic mass and ozone concentrations suggests that MO-OOA is associated with overall photochemical oxidant concentrations in the region, rather than being strongly driven by local daytime production, as was concluded for SOA in the Yangtze River Delta region in China (Wan et al., 2022).

In contrast to MO-OOA, LO-OOA showed a pronounced maximum in April (0.59 ± 0.72 μg m^{-3}, Fig. 1e), followed by a sharp decline in May (0.15 ± 0.17 μg m^{-3}, Fig. 1e). This peak in April coincided with the highest ozone concentrations (38 ± 4.7 ppb, Fig. 3a) during EPCAPE, supporting a strong contribution to LO-OOA formation from photochemical oxidation. Peak daily mean downwelling shortwave radiation (DSW) occurred during summer (235 ± 324 W m^{-2}, Table S7), but LO-OOA concentrations remained low, suggesting a reduction of photochemical efficiency by the increased local cloud fraction in May (0.69 ± 0.39, Fig. 3d). LO-OOA, however, showed correlations with DSW for 3 months whereas other factors correlated for 1 month at most (Fig. S7, Table S6). In contrast, MO-OOA showed correlations with ozone during 11 months of the year, with February being the only exception (Fig. S8, Table S6). This contrast suggests that LO-OOA is more strongly associated with local photochemical oxidation, while MO-OOA is more associated with regional photochemical processes. LO-OOA showed substantially larger normalized differences of 74–185% between the maximum and minimum hourly mean concentration throughout the year (compared to 31–65% for MO-OOA, Table S7) and a clearer midday maximum in spring, summer, and fall from 11:00 to 13:00 PT (Fig. 2m–o), overlapping with peaks in DSW (12:00–14:00 PT, Fig. 4, S4) and preceding the

https://doi.org/10.5194/egusphere-2026-4695
Preprint. Discussion started: 24 August 2026

ozone maximum (13:00–15:00 PT, Fig 4, S4). The close temporal peaks in LO-OOA, DSW, and ozone suggest LO-OOA formation is consistent with local daytime photochemical production. In winter, LO-OOA had two additional peaks in the morning (06:00–07:00 PT, Fig. 2l) and the evening (19:00–20:00 PT, Fig. 2m) that coincided with HOA peaks associated with traffic.

Similar to MO-OOA, C-OOA and HOA mass concentrations are highest in September (Fig. 1g,i) likely due to the wildfire influence from September 21 to 28. However, C-OOA and HOA mass concentrations remain relatively high into fall, whereas MO-OOA decreases by more than half from summer, averaging 0.70 ± 0.88 μg m^{-3} in fall (Table S7).

Fall is characterized by lower mean relative humidity but high variability (58.6% ± 24.8%, Table S7), consistent with more variable meteorological conditions and differences in back-trajectories as discussed in the next section. rBC increased during fall (57 ± 62 ng m^{-3}, Table S7) and winter (89 ± 152 ng m^{-3}, Table S7), showing a strong combustion influence that tracks closely with both C-OOA and HOA.

Although both are from combustion sources, the mass spectra of HOA and C-OOA reflect different degrees of oxidation. HOA shows clear morning and evening peaks for most seasons (Fig. 2v–x), consistent with traffic emissions, while rBC exhibits a similar morning maximum (07:00–12:00 PT, Fig. 4). High concentrations of HOA are associated with particle number size distributions with unimodal peaks at a smaller diameter (~30-40 nm, Fig. 1j) than for other PMF factors (~60-70 nm, Fig 1f,h). In contrast, C-OOA has no evident diurnal variation in any season, with a normalized difference between the maximum and minimum hourly mean concentration ranging from 49% to 79% (Table S7) compared to HOA at 66-130%, (Table S7). Only an 11% increase in C-OOA is observed overnight between 20:00 and 08:00 PT relative to daytime (08:00–20:00 PT; Fig. 4), which may be associated with the 10% higher nighttime relative humidity allowing for aqueous reactions to occur. However, a morning increase was not apparent during winter when C-OOA concentrations were lowest (0.09 ± 0.23 μg m^{-3}, Table S7), perhaps reflecting a substantial contribution from combustion sources that are mixed offshore by alternating land-sea breeze conditions. C-OOA showed no correlation with LCF or RH throughout most of the year, with only occasional weak negative relationships (Table S6). C-OOA showed the most consistent correlations with rBC over the year compared to the other oxygenated factors (Fig. S9, Table S6). In fall, C-OOA (1.36 ± 1.32 μg m^{-3}, Fig. 2t) and rBC (90 ± 112 ng m^{-3}, Fig. S4x) both peak at 11:00 to 12:00 PT, further supporting a similar combustion source during this season.

3.3 Back-Trajectory Differences in NR Organic Mass

CNW was the most frequent trajectory type overall during EPCAPE (63%), followed by LALB (19%), EAS (8%), SOU (7%), and MWE (3%). CNW trajectories were the most frequent from March through October, accounting for 56–93% of trajectories

https://doi.org/10.5194/egusphere-2026-4695
Preprint. Discussion started: 24 August 2026

(Han et al., 2025). In contrast, LALB trajectories reached their highest frequency in December (42%), EAS peaked in November (33%), while SOU (15%) and MWE (17%) were most frequent in February 2024.

The CNW trajectories were associated with elevated concentrations of MO-OOA (0.79 ± 1.44 μg m^{-3}, Fig. 5b) and SR-OOA (0.23 ± 0.22 μg m^{-3}, Fig. 5a) along with higher UCVF (0.57 ± 0.23, Fig. 6) than the EPCAPE average and other back-trajectories. The co-occurrence of high UCVF and mass concentrations of MO-OOA and SR-OOA, both of which exhibit the highest O/C ratios (1.47 and 1.00, respectively, Table S3) of the PMF factors, support that cloud aqueous oxidation associated with over-ocean trajectories plays an important role in the formation of these highly oxidized components (Xu et al., 2017). Consistent with this interpretation, most CNW trajectories occurred during spring and summer, aligning with periods of greater cloud influence and photochemical activity, as well as higher concentrations of MO-OOA and SR-OOA.

The MWE trajectory included largely marine conditions and had the lowest mass concentrations for rBC (Fig. 6f) and all organic PMF factors (Fig. 5), with the exception being SR-OOA (Fig. 5a), supporting the interpretation of the m/z 78, 79, and 96 as MSA-related fragments from oxidation of marine biogenic DMS emissions. These air masses had relatively low nitrate and rBC concentrations, reflecting minimal continental input (Han et al., 2025).

In contrast, continental air masses showed higher concentrations of combustion-related factors. The LALB, SOU, and EAS trajectories were all associated with increased C-OOA (6–54%, Fig. 5d), HOA (46–61%, Fig. 5e), and rBC (27–97%, Fig. 6f) when compared to the EPCAPE average, indicating strong influence from anthropogenic emissions over land. Differences in HOA across these continental trajectories were not statistically significant, suggesting similar source types, while C-OOA concentrations were comparable between LALB and EAS based on a Welch's two-sample t-test. The higher concentrations of HOA and rBC for LALB and EAS trajectories relative to other trajectories support a large contribution from combustion-related sources, with C-OOA reflecting a mixture of combustion emissions and subsequent oxidation.

Among the continental back-trajectories, EAS back-trajectories showed the most distinct meteorological conditions, characterized by the lowest average RH (40 ± 19%), LCF (0.30 ± 0.36), and UCVF (0.20 ± 0.09), and the highest average DSW (201 ± 254 W m^{-2}), ozone (39.6 ± 8.0 ppb), and rBC concentrations (107.16 ± 175.31 ng m^{-3}) (Fig. 6). These conditions indicate a predominantly dry and photochemically oxidizing environment. The high organic mass concentrations observed during these periods are therefore unlikely to be driven by aqueous-phase reactions. SR-OOA concentrations were lowest for EAS trajectories (0.02 ± 0.03 μg m^{-3}, Fig. 5a), further supporting the limited role of in-cloud aqueous reactions in EAS air masses. These trajectories occurred primarily during the fall and winter months (October through February).

The SOU trajectory showed 21% lower ozone (28.3 ± 8.0 ppb, Fig. 6c), 31% lower DSW (131 ± 216 W m^{-2}, Fig. 6d), and 21% higher LCF (0.66 ± 0.39, Fig. 6e) than the campaign average, indicative of reduced photochemical activity due to local

https://doi.org/10.5194/egusphere-2026-4695
Preprint. Discussion started: 24 August 2026

cloudiness. As a result, LO-OOA concentrations were 17% lower in these air masses (0.19 ± 0.34 μg m^{-3}, Fig. 5c) than the EPCAPE average. The lower LO-OOA in SOU air masses suggests that LO-OOA formation is closely tied to photochemical production and is limited under conditions of low solar radiation.

3.4 Comparisons with Vapor-Phase Organic Acids

The mixing ratios of gas-phase organic acids measured by CIMS from April 30 through June 6 span several orders of magnitude (Table S8). Several organic acids show distinct diurnal cycles (Fig. S10) and significant correlations to oxygenated AMS NR PMF factors (Table S9) and tracers for mixed combustion and oxidation processes (Table S10). HOA did not display significant correlations with any of the measured acids (R = -0.04–0.15, Table S9), consistent with its interpretation as a relatively recently-emitted and less-oxidized factor. Of the 27 calibrated organic acids, 21 acids contained correlations (|R| > 0.25) to AMS NR PMF factors.

Only LO-OOA correlated with butyric (BUT), cyanoacetic (CYAA), 2-hydroxyisocaproic (HCA), hexanoic (HEX), propanetriol (PTL), pyruvic (PYA), and valeric (VA) acids (R = 0.26–0.38, Table S9). These acids generally exhibited diurnal cycles characterized by a daytime maximum (Fig. S10b–d), suggesting associations with less-aged secondary organic aerosol formed through photochemical oxidation. PTL showed a slightly delayed afternoon maximum relative to the other acids, suggesting formation through more aged or multistep photochemical reactions, and was correlated to DSW (R = 0.29, Table S10). HCA was also correlated with DSW (R = 0.30, Table S10) in addition to rBC (R = 0.29, Table S10), suggesting that its formation is linked to photochemical oxidation of combustion-related emissions. VA and CYAA were positively correlated with O_3 (R = 0.28–0.34, Table S10), further supporting photochemical production of LO-OOA. The diurnal cycle of CYAA closely resembled that of ozone, with a morning minimum likely driven by titration under recent NO emissions followed by an afternoon maximum delayed relative to the midday peak in DSW (Fig. S10d), supporting formation by photochemical reactions. PYA correlated to both DSW and O_3 (R = 0.28–0.42, Table S10), consistent with previous observations that it can form rapidly through photochemical reactions of urban emissions (Veres et al., 2011). Previous studies have also identified BUT and VA as both primary and secondary products of automobile exhaust (Mattila et al., 2018;Friedman et al., 2017). However, BUT did not exhibit significant correlations with photochemical tracers or rBC, despite its proposed traffic-related origin. Similarly, HEX, which has previously been associated with cooking emissions (Jiang et al., 2025), did not exhibit correlations with any tracers and had only a weak diurnal cycle (Fig. S10e). Collectively, these results suggest that many of the measured acids are linked to daytime photochemical reactions that likely stem from anthropogenic emissions, similar to LO-OOA.

Among all measured acids, glyoxylic acid (GYLA) had the strongest correlation with UCVF (R = 0.43, Table S10) and was most strongly associated with the more oxygenated PMF factors MO-OOA (R = 0.58, Table S9) and SR-OOA (R = 0.39,

https://doi.org/10.5194/egusphere-2026-4695
Preprint. Discussion started: 24 August 2026

Table S9). These relationships suggest that GYLA is strongly influenced by aqueous-phase oxidation during transport within cloud-processed air masses, consistent with the interpretation of SR-OOA and MO-OOA as factors linked to cloud and multiphase reactions. Liu et al. (2012) have similarly reported enhanced concentrations of small organic acids, including glyoxylic acid, following aqueous-phase reactions, supporting the interpretation that GYLA formation is associated with cloud-related oxidation pathways.

C-OOA was the only PMF factor that had correlations with 1,2,4-butanetriol (BTL), 2-furoic (FUA), and pinonic (PINA) acids (R = 0.26–0.32, Table S9). Among these acids, PINA has been identified as a product of α-pinene oxidation with O_3 or OH (Cheng et al., 2004;Kolodziejczyk et al., 2019;Hoffmann et al., 1998;Hakola et al., 1994;O'Dowd et al., 2002) and as a precursor of biogenic secondary aerosol in forested areas (Kavouras et al., 1998, 1999). PINA has also been associated with biomass burning tracers such as levoglucosan (Cheng et al., 2011), consistent with the interpretation of C-OOA as an aged continental factor influenced in part by biomass burning emissions. However, the diurnal cycle of PINA showed a pronounced morning maximum near 08:00 local time that closely aligned with the morning peak in rBC concentrations. PINA was positively correlated with rBC (R = 0.32, Table S10), suggesting that combustion emissions, potentially related to biomass burning, may contribute to its temporal variability. Tong et al. (2022) also reported that less-oxygenated and more volatile terpene oxidation products, including PINA, preferentially partitioned into the particle phase during nighttime cooling conditions. However, no significant relationship between PINA and temperature was observed during EPCAPE (R = 0.02, Table S10).

4 Multivariate Regression Analyses

These results showing the relationships of PMF factors with sources and oxidation tracers provide evidence that both photochemical and aqueous-phase oxidation contribute to secondary organic aerosol formation during EPCAPE. To further quantify the relative contribution from these pathways of secondary and primary formation, MLR was performed using ozone, UCVF, RH, LCF, and rBC to predict the O/C ratio as well as the more oxidized PMF factors (SR-OOA, MO-OOA, LO-OOA, C-OOA). Additional analyses supporting the use of ozone as a photochemical tracer, including comparisons with DSW, cloud fraction, and odd oxygen ($O_X = O_3 + NO_2$), are included in Text S1 (Figs. S11–S13; Tables S11–S12).

4.1 O/C Variability Largely Explained by RH and O_3

For O/C, ozone, UCVF, RH, LCF, and rBC explain the variability very well (R^2 = 0.97, Table 1). Relative humidity explains 39% and ozone explains 38% of the variability in O/C, while UCVF accounts for a smaller share (19%). Figure 7a displays the annual model performance for O/C, while Figure 7f highlights the strong relationships between O/C and RH during spring

https://doi.org/10.5194/egusphere-2026-4695
Preprint. Discussion started: 24 August 2026

as well as ozone during fall. In contrast, LCF shows a slight negative contribution (-2%), indicating minimal local cloud influence. The higher contribution from UCVF than LCF suggests that aqueous reactions occurring upwind play a larger role than local in-cloud aqueous reactions. As expected for a metric of SOA formation, O/C shows only a negligible contribution from the mixed combustion tracer rBC (2%).

Ozone has a stronger contribution to variability during winter (58%) and fall (70%), and a smaller role during spring (15%) and summer (30%). The lower spring (15%) and summer (33%) contributions from ozone coincide with increased cloudiness (LCF = 0.62 ± 0.40-0.42, Table S7), which suppress photolysis rates and limit photochemical oxidation. During spring, LCF shows a stronger, but relatively small, influence (−9%), further supporting the role of local cloud conditions in modulating oxidation pathways. In contrast, relative humidity contributes more during spring (52%) and summer (56%), aligning with enhanced aqueous-phase reactions under more humid conditions.

The size dependence of oxidized organic aerosol provides additional insight into the mechanisms contributing to organic oxidation (Fig. 8). Across all seasons, AMS NR m/z 44 (Fig. 8a–e) and total organic aerosol (Fig. 8f–j) showed similar accumulation-mode size distributions, generally peaking between ~300 and 700 nm. In addition, the mass ratio of AMS NR m/z 44 to AMS NR organics, equivalent to f_{44} and commonly used as a unit-mass-resolution (UMR) proxy for O/C, remained relatively constant with particle size (Fig. 8k–o), while the ratio of AMS NR Org to AMS NR mass concentration generally decreased with increasing diameter (Fig. 8p–t). These relationships are consistent with theoretical expectations for surface-limited condensation, in which oxygenated organic fragments are added proportionally across particle sizes while the contribution of organic mass decreases relative to particle mass with increasing diameter (Liu et al., 2011;Maria et al., 2004). Similar size-dependent behavior was previously observed during a late summer study (15 August–1 October) at Scripps Pier in 2009 (Liu et al., 2011). Here these relationships persist across all seasons, suggesting that surface-limited condensation of oxidized organic aerosol is a consistent feature of the organic aerosol formation in coastal Southern California. Seasonal differences in the mode peak diameter and magnitude were also observed, with larger mode peak diameters and higher concentrations in the accumulation-mode m/z 44 and organic aerosol during spring and summer, consistent with greater oxidation rates under more humid and cloud-influenced conditions (Farley et al., 2023). Figure S14 shows the contribution from organic PMF factors to O/C, which highlights a large contribution from MO-OOA, LO-OOA, and C-OOA throughout the year.

When isolating CNW back-trajectories, thereby minimizing variability associated with different air mass sources, the contribution from aerosol-phase aqueous reactions described by RH increases to 47%, and the contributions of the other variables are lower (Table 1). This consistency in how much RH contributes to O/C, followed by O_3 then UCVF for CNW trajectories and across all trajectories suggests that the processes responsible for organic oxidation are similar among different air mass regimes.

https://doi.org/10.5194/egusphere-2026-4695
Preprint. Discussion started: 24 August 2026

4.2 SR-OOA and Upwind Cloudiness

UCVF accounts for 70% of SR-OOA mass concentration variability, while RH contributes only 14% to the explained variability (Table 1). The ozone contribution is negative (-11%, Table 1) as is LCF (-5%, Table 1), also showing weak dependence on local variables. Maneenoi et al. (2025) found that NSS sulfate formation was not strongly associated with metrics for local in-cloud aqueous oxidation such as LCF or LWC, which they attributed to SO_2 likely already being depleted during transport before reaching the site. Although DMS was not measured directly here, the similar marine biogenic origin of DMS oxidation products suggests that MSA precursors may also have been depleted during transport, limiting local cloud aqueous reactions of SR-OOA at the site. This is consistent with the small negative contribution from LCF, while the much larger contribution from UCVF indicates that SR-OOA formation is more strongly associated with upwind cloud aqueous reactions occurring prior to arrival at the site. Therefore, these relationships indicate that SR-OOA is primarily associated with in-cloud aqueous reactions occurring upwind rather than local cloud effects, with minimal evidence for direct photochemical production or aerosol water oxidation.

SR-OOA also differs from AMS NR sulfate during EPCAPE, where photochemical oxidation (34%, Table 1) and aerosol aqueous (36%, Table 1) reactions contributed more strongly to sulfate formation than upwind cloud-associated oxidation (29%, Table 1) (Maneenoi et al., 2025). The stronger dependence on UCVF for SR-OOA suggests that cloud aqueous reactions are particularly important for the formation of sulfur-containing organic aerosol components such as MSA (Ge et al., 2012;Barnes et al., 2006). This interpretation is consistent with previous estimates that approximately 74% of MSA formation occurs in clouds at high liquid water conditions (Chen et al., 2018).

Restricting the analysis to CNW trajectories produces little change (≤6%, Table 1) in the relative contributions for SR-OOA, indicating that the relationship with upwind aqueous reactions remains. The contribution from ozone to SR-OOA for CNW trajectories decreases in magnitude from -11% to -5%, indicating that part of the small negative annual contribution is associated with differences in source regions. The remaining contribution (-5%) is negligible and therefore, not interpreted further. For seasonal models, UCVF represents the largest contribution to SR-OOA in spring, summer, and fall. Consistent with the previously observed spring maximum in UCVF, spring also showed the strongest SR-OOA MLR model performance, with an R^2 of 0.75 (Table 1). Figure 7b displays the springtime model performance for SR-OOA, while Figure 7g highlights the relationship between SR-OOA and UCVF during spring. The exception to this is during winter, when UCVF is lowest (0.29 ± 0.12, Table S7) and ozone becomes the largest contributor (55%) to explaining SR-OOA variability. However, despite this larger ozone contribution, model performance decreases from an annual R^2 of 0.64 to 0.55 in winter (Table 1), suggesting that SR-OOA variability is less explained when cloud influence is reduced. Overall, the annual average absolute contributions shown in Figure 9b are similar for all four seasons under conditions with sufficient cloud influence, consistent with the minimal changes observed when restricting the analysis to CNW trajectories.

https://doi.org/10.5194/egusphere-2026-4695
Preprint. Discussion started: 24 August 2026

The monthly correlations for SR-OOA were generally consistent with the seasonal MLR contributions for ozone and UCVF (Fig. 10a). The monthly correlations quantify the pairwise associations between each tracer and OOA factor, whereas MLR quantifies their independent contributions after accounting for the other predictors simultaneously (Roustaei, 2024). The stronger monthly correlations with either ozone or UCVF generally corresponded to larger seasonal MLR contributions from the same tracer. SR-OOA exhibited larger MLR contributions from and stronger regression correlations with UCVF than ozone in spring, summer, and fall, consistent with formation by in-cloud aqueous reactions during periods of high upwind cloudiness. This agreement indicates that the relationships identified by the simple regressions remained evident in MLR. Although a weak, negative correlation of SR-OOA and UCVF is observed in September ($R = -0.38$), stronger regression correlations with UCVF in July ($R = 0.47$) and August ($R = 0.41$) than with ozone ($R = 0.27–0.32$) when SR-OOA mass concentrations are highest results in the larger MLR contribution of UCVF to SR-OOA formation than ozone in summer. SR-OOA was not significantly correlated with UCVF in January or February ($p > 0.05$), and all regression correlations with both UCVF and ozone remained below the threshold for a weak correlation ($|R| < 0.25$). The strongest winter regression correlations were with ozone in February and March ($R = 0.18–0.22$, Table S6), resulting in ozone providing the largest MLR contribution to explaining variability in SR-OOA formation during winter. However, these limited tracer associations likely contributed to the reduced winter MLR model performance.

4.3 Differing Influences on LO-OOA and MO-OOA

LO-OOA has the highest contribution from ozone, which accounts for 64% of LO-OOA variability, while RH and UCVF contribute negatively (-19% and -13%, respectively, Table 1). Contributions from rBC (2%) and LCF (-5%) are comparatively minor (Table 1). These relationships indicate that LO-OOA formation is primarily associated with photochemical oxidation, consistent with oxidation of anthropogenic organic precursors associated with fossil fuel emissions in coastal Southern California (Liu et al., 2011), with limited influence from aerosol or cloud aqueous oxidation pathways. Ozone remains the largest contributor to LO-OOA across all seasons (36–57%, Table 1), indicating a persistent photochemical role. The strongest model performance occurred during spring, when ozone concentrations were highest (39.1 ± 7.2 ppb, Table S7), suggesting enhanced photochemical activity contributed to the improved ability of the model to capture LO-OOA variability ($R^2 = 0.56$, Table 1). Figure 7d displays the springtime model performance for LO-OOA, while Figure 7i highlights the relationship between LO-OOA and ozone during spring. The relatively small seasonal changes in LO-OOA contributions further suggest that the annual average absolute contributions shown in Figure 9b are representative of LO-OOA formation throughout the year. These large seasonal contributions from ozone are consistent with the stronger monthly correlations when compared to UCVF (Fig 10b). Although the strongest correlation with either UCVF or ozone in spring occurred with UCVF in May ($R = 0.41$), this relationship was offset by an opposing trend with UCVF in April ($R = -0.26$) and a non-significant correlation in

https://doi.org/10.5194/egusphere-2026-4695
Preprint. Discussion started: 24 August 2026

June, likely reflecting the variability in sources and meteorology in the spring. In contrast, ozone remained positively correlated with LO-OOA from April through June (R = 0.23–0.41), resulting in the larger seasonal contribution from ozone to LO-OOA.

RH (31%) and UCVF (26%) together contribute more strongly to MO-OOA than ozone (14%) (Table 1), indicating a larger role for aqueous reactions for MO-OOA compared to LO-OOA, consistent with a prior study (Yao et al., 2022). A positive contribution from rBC (15%, Table 1) suggests an association with aged combustion-related aerosol, consistent with a more oxidized and transported aerosol component. However, this model captures the least variability (R^2 = 0.27, Table 1), representing the lowest explanatory power among all PMF factors in the annual analysis. MLR for separate seasons yields higher R^2 values (R^2 = 0.51–0.71, Table 1), indicating improved predictive skill when variability in sources and meteorology is more limited.

The importance of aqueous reactions within clouds for MO-OOA is most apparent during spring, when UCVF contributes 48% (Table 1) and upwind cloudiness is high (0.64 ± 0.24, Table S7). Spring also corresponds to the highest model performance for MO-OOA (R^2 = 0.71, Table 1), as shown in Figure 7c. Figure 7h highlights the relationships between MO-OOA with UCVF and ozone, which was the second largest contributor to MO-OOA (23%), during spring. These spring contributions are consistent with the monthly correlations for MO-OOA (Fig. 10c). While both ozone and UCVF have positive monthly correlations with MO-OOA throughout spring, MO-OOA exhibited a stronger seasonal correlation with UCVF (R = 0.45, Table S13) than with ozone (R = 0.25, Table S13) which included the strongest monthly correlation in spring with UCVF in May (R = 0.66). This resulted in a larger contribution from UCVF than ozone in spring.

A negative contribution from UCVF is observed during summer for MO-OOA (-35%, Table 1) as well as LO-OOA (-36%, Table 1). For MO-OOA, excluding the September fire event decreased the contribution from UCVF to only -9% (Table S14), increased the contribution from ozone from 46% (Table 1) to 71% (Table S14), and improved the model performance (ΔR^2 = 0.12, Table S14). Excluding the fire event similarly increased the correlation of UCVF and MO-OOA from -0.13 (Table S6) to 0.23 in September. Together, these results indicate that the apparent inverse relationship between UCVF and MO-OOA during summer is driven by the wildfire period, while photochemical oxidation is more strongly associated with MO-OOA formation during non-fire conditions. In contrast, the UCVF contribution for LO-OOA changed by only ~8% (from -36% to -28%), indicating that the inverse relationship with UCVF was largely unaffected by the wildfire period. This behavior is consistent with MO-OOA representing a more regionally transported, highly oxidized aerosol that was more strongly influenced by the wildfire event, during which MO-OOA was not adequately predicted. LO-OOA is driven by local photochemical oxidation, resulting in a more persistent inverse relationship with upwind and local cloudiness because cloud cover limits the solar radiation required for its formation.

https://doi.org/10.5194/egusphere-2026-4695
Preprint. Discussion started: 24 August 2026

Across all seasons, ozone contributions to MO-OOA formation are substantially higher in the MLR by season (23–77%) than annually (14%), while RH contributions decrease relative to the annual model. This shift likely reflects the negative correlation between ozone and RH within the dataset (R = -0.40), where photochemical and aqueous conditions partially offset one another in the annual analysis. When separated by season, these influences become more clearly resolved, with ozone providing the largest seasonal contribution during winter, summer, and fall when monthly correlations of MO-OOA with UCVF were weaker or non-significant (Fig. 10c). These seasonal contributions to variability as well as the seasonal differences in the average absolute contributions to MO-OOA mass are summarized in Figure 9c.

Under CNW trajectories, MO-OOA also shifts toward stronger photochemical and combustion-related influence. The contribution from RH decreases from 31% to 19%, and UCVF shifts from a positive contribution (26%) to slightly negative (-2%) (Table 1), indicating a reduced influence of aqueous reactions, that is also observed for LO-OOA and C-OOA. At the same time, the contribution from ozone increases from 14% to 32% (Table 1), and rBC increases from 15% to 38% (Table 1), showing a larger fraction of variability explained by photochemical oxidation concomitant with a greater influence from combustion-related sources. Despite this increasing contribution from rBC, the oxygenated nature of MO-OOA is consistent with a higher degree of oxidation than would be expected from recently emitted organic components. Relative to the annual model that includes all trajectories, the model performance improves slightly (R^2 increases from 0.27 to 0.33, Table 1), suggesting that factors not included in the MLR model have less influence when restricting to CNW back-trajectories.

4.4 C-OOA Reflects Large Seasonal Differences

In the annual MLR model, RH provides the largest contribution at 53% to C-OOA variability, while rBC also contributes 26% (Table 1). Ozone (2%) and UCVF (1%) contribute negligibly, and LCF contributes negatively (-17%) (Table 1), perhaps reflecting the role of local cloud-related losses such as scavenging (Zhang et al., 2024). Together, these relationships suggest that C-OOA is influenced by combustion-related precursor emissions that subsequently undergo aqueous reactions under humid conditions. Although RH is the largest contributor in the annual model, the highest and most variable C-OOA concentrations occur during periods of relatively low RH in fall and winter, when EAS, SOU, and LALB (continental) influences are more prevalent. This suggests that the availability of combustion-related precursors is a key controlling factor for C-OOA formation, while RH is likely responsible for the subsequent oxidation of these emissions once present. Consequently, elevated RH appears to promote secondary formation of combustion-derived aerosol rather than directly driving periods of maximum C-OOA concentration. Additionally, the limited influence of local cloud aqueous reactions for C-OOA, as well as MO-OOA (<5%), is consistent with Farley et al. (2026) who found no increase in either C-OOA and MO-OOA mass concentrations in cloud droplet residuals compared to ambient concentrations.

https://doi.org/10.5194/egusphere-2026-4695
Preprint. Discussion started: 24 August 2026

In the seasonal models, ozone provides the largest positive contribution to C-OOA during summer (37%) and fall (43%), with MLR model R^2 increasing from 0.45 annually to 0.68 in summer and reaching a maximum of 0.77 in fall (Table 1). Consistent with these contributions, Figure 10d shows stronger monthly correlations between C-OOA and ozone than with UCVF for these seasons, directly contrasting SR-OOA which had a stronger association with UCVF. The strong fall MLR model performance (Figure 7e) highlights the relationships among C-OOA, ozone, and rBC during fall (Figure 7j). In winter, rBC has the largest contribution (49%, Table 1) and the MLR model performs well ($R^2 = 0.62$, Table 1), indicating that combustion-related influences are more consistently captured during this period. UCVF and ozone exhibited a range of different correlation strengths with C-OOA during winter, with individual monthly correlations indicating positive, negative, and non-significant relationships in January, February, and March. As a result, both tracers accounted for relatively small contributions to C-OOA formation, with ozone explaining 13% and UCVF 16% of the seasonal variability (Fig. 10d). In contrast, spring exhibits the lowest MLR model performance ($R^2 = 0.34$), although with large contributions from RH (37%) and UCVF (25%) (Table 1). This likely reflects a limitation in the model during spring, as C-OOA and rBC concentrations are lowest (0.09 ± 0.23 μg m^{-3} and 23 ± 35 ng m^{-3}, respectively, Table S7), reducing the signal-to-noise ratio and making variability more difficult to capture. As a result, although aqueous and cloud-related reactions appear important, their influence is less well resolved.

For CNW conditions, rBC contributions increase from 26% to 35%, while UCVF becomes more negative (-15%) (Table 1). This trend indicates that even within the predominantly marine CNW regime, C-OOA is not associated with periods of greater upwind in-cloud aqueous reactions but instead reflects combustion-related aerosol, including potential biomass burning contributions. One possible explanation is that scavenging by upwind clouds reduces C-OOA concentrations, while regional combustion processes replenish C-OOA concentrations. Despite these changes, the contribution from ozone remains negligible under CNW conditions (-2%), indicating that photochemical oxidation is not the main driver of annual C-OOA variability.

Overall, C-OOA represents a factor influenced by combustion-related emissions and photochemical and aqueous reactions, with the relative importance of photochemical, aqueous, and primary influences varying substantially by season and transport regime (Figure 9c).

5 Conclusions

This study characterizes the sources, variability, and formation pathways of submicron organic aerosol at a coastal site in Southern California using high-resolution AMS measurements, PMF analysis, trajectory clustering, and multilinear regression. Five organic aerosol factors were resolved, including one primary factor (HOA) and four oxygenated factors (SR-OOA, MO-OOA, LO-OOA, and C-OOA), each exhibiting distinct chemical signatures and time-varying behavior.

https://doi.org/10.5194/egusphere-2026-4695
Preprint. Discussion started: 24 August 2026

Seasonal and diurnal patterns highlight the differing roles of photochemical and aqueous reactions. LO-OOA displays midday maxima coincident with ozone and solar radiation, consistent with the role of photochemical oxidation, whereas SR-OOA and MO-OOA mass concentrations are larger in cloud conditions, particularly for SR-OOA during spring (0.20 ± 0.14 μg m^{-3}) and summer (0.38 ± 0.26 μg m^{-3}) when UCVF is highest (0.61–0.64 ± 0.20–0.24). Similar to MO-OOA, C-OOA exhibits lower diurnal variability than other PMF factors. C-OOA concentrations are 11% higher from 20:00 to 08:00 PT than from 08:00 to 20:00 PT, consistent with aged combustion-related aerosol influenced by transport and other atmospheric processes. The overnight 11% increase also coincides with a 10% increase in RH, suggesting that aqueous reactions may contribute to the oxidation of combustion-related aerosol. This overnight increase was not observed during winter, consistent with the negligible RH contribution during winter (-5%) relative to the larger RH contributions observed during spring through fall (18–37%). These patterns indicate that aqueous-phase reactions contribute to the formation and oxidation of organic aerosol at high relative humidity (RH > 75%) and increasing upwind cloudiness (UCVF > 50%). HOA shows clear diurnal patterns consistent with local traffic emissions, consistent with a combustion-related source.

Back-trajectory analysis reveals that marine and continental air masses contribute distinct sources of organic components. Coastal northwesterly trajectories exhibited the highest concentrations of MO-OOA (0.79 ± 1.44 μg m^{-3}) and SR-OOA (0.23 ± 0.22 μg m^{-3}) alongside the highest UCVF (0.57 ± 0.23), supporting an important role of upwind cloud aqueous reactions in forming highly oxidized aerosol. In contrast, continental air masses (LALB, SOU, EAS) are associated with 46–61% higher HOA, 6–54% higher C-OOA, and 27–97% higher rBC mass concentrations when comparing to the EPCAPE average, reflecting combustion-related emissions. Compared to the EPCAPE average, LO-OOA concentrations were 17% lower during southerly back-trajectories associated with reduced ozone (-21%) and DSW (-31%) and enhanced local cloudiness (+21%), further supporting a strong dependence of LO-OOA on photochemical production.

The oxidation state of organic aerosol, represented by O/C, reflects the combined influence of photochemical and aqueous reactions. Multivariate linear regression shows that O/C is well explained (R^2 = 0.97) by a combination of ozone (38%) representing photochemical oxidation and relative humidity (39%) representing aerosol water aqueous oxidation. Upwind cloud influence represented as UCVF provides a smaller contribution (19%), while local cloud fraction and mixed combustion tracers play minimal roles (<5%). These results indicate that organic aerosol oxidation at this site is influenced by both photochemical and aqueous-phase reactions, with larger contributions from upwind rather than local cloud effects.

The organic PMF factors identified at EPCAPE show associations with different oxidation mechanisms. Monthly correlations to oxidative and mixed-combustion tracers are broadly consistent with contributions resolved from multilinear regression. SR-OOA, which contains fragments related to MSA, is strongly correlated with sulfate (R = 0.85), moderately correlated with UCVF (R = 0.52), and weakly correlated to SST (R = 0.43), indicating both co-emission with marine biogenic precursors and oxidation associated with upwind clouds. Consequently, higher SR-OOA concentrations co-occur with bimodal size

https://doi.org/10.5194/egusphere-2026-4695
Preprint. Discussion started: 24 August 2026

distributions, consistent with cloud-related oxidation of organic precursors contributing to particle growth. Consistent with simple regression correlations, MLR attributed 70% of SR-OOA formation to upwind in-cloud aqueous reactions. LO-OOA reflected local photochemical production with an annual correlation to ozone (R = 0.37), significant correlations with solar radiation for three months compared to only up to one month for the other OOA factors, and a 64% photochemical contribution from the annual MLR analysis. MO-OOA has a larger MLR contribution from UCVF during spring (48%) and larger ozone contributions during summer (46%), fall (77%), and winter (44%), indicating that in-cloud aqueous reactions and photochemical oxidation vary with meteorological conditions. Correlations from simple regressions further support these seasonal differences, with stronger springtime correlations to UCVF than ozone, including the highest monthly correlation in May (R = 0.66), corresponding to larger UCVF contributions, but stronger correlations during winter, summer, and fall with ozone (R = 0.12–0.76) than with UCVF (R = -0.13–0.38) coincided with the larger seasonal ozone MLR contributions. Similar to MO-OOA, C-OOA formation pathways varied by season, with refractory black carbon contributing most to MLR during winter (49%), larger RH (37%) and UCVF (25%) contributions during spring, and greater ozone contributions during summer (37%) and fall (43%). Annual correlations with refractory black carbon (R = 0.33) and biomass burning tracers, including nss-K (R = 0.55), XRF Br (R = 0.79), and CIMS HNCO (R = 0.28), indicate a combustion-related influence, while consistently positive ozone correlations during summer (R = 0.17–0.48) and fall (R = 0.04–0.50) support enhanced photochemical formation during these seasons.

Previous studies investigating the photochemical and aqueous reactions of organic aerosols have primarily evaluated MO-OOA and LO-OOA, often using O_X as an indicator for photochemical oxidation and RH or ALWC for aqueous-phase oxidation (Table S1). This study extends these approaches by distinguishing aerosol water aqueous oxidation from local and upwind in-cloud aqueous oxidation using LCF and UCVF and by examining these pathways for SR-OOA and C-OOA in addition to MO-OOA and LO-OOA. Accounting for upwind cloud aqueous reactions is particularly important at this site, where more oxidized SOA factors had stronger associations with upwind rather than local cloud aqueous reactions, which would not be captured by local cloud measurements alone. In contrast, local cloudiness coincided with reduced ozone and LO-OOA concentrations, consistent with reduced photochemical oxidation. MLR analysis accounts for covariability among oxidation tracers and provides quantitative estimates of their relative contributions to organic aerosol formation and oxidation. However, the predictors used represent broader oxidation processes and do not identify the individual chemical reactions responsible for secondary organic aerosol formation, which would require more comprehensive measurements of oxidants and VOCs over longer timescales.

Overall, these results demonstrate that SOA formation reflects both photochemical and aqueous oxidation pathways whose relative importance depends strongly on aerosol source type, season, and transport history. Figure 11 summarizes these relationships by displaying the seasonal organic PMF factor composition together with corresponding seasonal correlations and MLR contributions for each of the major formation pathways. SR-OOA and MO-OOA are more strongly linked to regional

https://doi.org/10.5194/egusphere-2026-4695
Preprint. Discussion started: 24 August 2026

cloud influence and aqueous reactions, whereas LO-OOA is more consistently associated with local photochemical production. In contrast, C-OOA reflects mixed combustion-related sources that vary seasonally with changing photochemical and aqueous conditions while HOA is linked to combustion based on the annual and seasonal correlations to rBC. Together, these results quantify the contributions of photochemical and upwind cloud aqueous reactions to shaping the oxidation state and composition of coastal organic aerosol. The differences in organic aerosol oxidation are relevant to aerosol-cloud interactions since O/C is commonly used to parameterize the hygroscopicity of organic aerosols (Lambe et al., 2011;Chang et al., 2010). Representing these oxidation pathways and their contributions to organic aerosol formation and oxidation state is therefore important for representing SOA formation and the ability of organic-containing particles to serve as cloud condensation nuclei in coastal environments.

Data availability

All data collected during EPCAPE are publicly available. Scripps and collaborator measurements are available from https://doi.org/10.6075/J0NG4QT4 (Russell et al., 2023). DOE ARM data were obtained from the Atmospheric Radiation Measurement (ARM) User Facility, a U.S. Department of Energy (DOE) Office of Science user facility managed by the Biological and Environmental Research Program: https://adc.arm.gov/discovery/results/s::epcape.

Author contributions

VZB and LMR conceptualized the project and led the interpretation of the measurements. VZB performed the formal analysis and drafted the manuscript. VZB, LMR, JLD, ASW, SH, DL, and RF contributed to data curation from the Mt. Soledad instruments. JW and JL led collection, curation, and interpretation of CIMS measurements. LMR, JW, and AA acquired funding for the project. All authors reviewed and edited the manuscript.

Acknowledgements

This research was supported by the Atmospheric Radiation Measurement (ARM) User Facility, a U.S. Department of Energy (DOE) Office of Science user facility managed by the Biological and Environmental Research Program. The authors would like to additionally acknowledge Dr. Markus Petters.

https://doi.org/10.5194/egusphere-2026-4695
Preprint. Discussion started: 24 August 2026

Competing interests

At least one of the (co-)authors is a member of the editorial board of Atmospheric Chemistry and Physics.

Financial support

This work was funded by the U.S. Department of Energy's Atmospheric System Research, an Office of Science Biological and Environmental Research program, under Grant DE-SC0022958 and by the National Science Foundation under Grant AGS-2133441.

References

Aldworth, T., Buettner, W. C., Greiner, S. M., Beeton, T., and Schultz, C. A.: Implementing the Incident Strategic Alignment Process on the 2023 Six Rivers Lightning Complex, Colorado Forest Restoration Institute, Colorado State UniversityCFRI-2413, 2024.

Alfarra, M., Prevot, A., Szidat, S., Sandradewi, J., Weimer, S., Lanz, V., Schreiber, D., Mohr, M., and Baltensperger, U.: Identification of the mass spectral signature of organic aerosols from wood burning emissions, Environmental Science and Technology, 41, 5770-5777, 10.1021/es062289b, 2007.

Ault, A., Moore, M., Furutani, H., and Prather, K.: Impact of Emissions from the Los Angeles Port Region on San Diego Air Quality during Regional Transport Events, ENVIRONMENTAL SCIENCE & TECHNOLOGY, 43, 3500-3506, 10.1021/es8018918, 2009.

Barnes, I., Hjorth, J., and Mihalopoulos, N.: Dimethyl sulfide and dimethyl sulfoxide and their oxidation in the atmosphere, Chemical Reviews, 106, 940-975, 10.1021/cr020529+, 2006.

Barth, M., Hess, P., and Madronich, S.: Effect of marine boundary layer clouds on tropospheric chemistry as analyzed in a regional chemistry transport model, JOURNAL OF GEOPHYSICAL RESEARCH-ATMOSPHERES, 107, 10.1029/2001JD000468, 2002.

Bates, T. S., Quinn, P. K., Frossard, A. A., Russell, L. M., Hakala, J., Petaja, T., Kulmala, M., Covert, D. S., Cappa, C. D., Li, S. M., Hayden, K. L., Nuaaman, I., McLaren, R., Massoli, P., Canagaratna, M. R., Onasch, T. B., Sueper, D., Worsnop, D. R., and Keene, W. C.: Measurements of ocean derived aerosol off the coast of California, Journal of Geophysical Research-Atmospheres, 117, 10.1029/2012jd017588, 2012.

Berta, V. Z., Russell, L. M., Price, D. J., Chen, C. L., Lee, A. K. Y., Quinn, P. K., Bates, T. S., Bell, T. G., and Behrenfeld, M. J.: Non-volatile marine and non-refractory continental sources of particle-phase amine during the North Atlantic Aerosols and Marine Ecosystems Study (NAAMES), Atmospheric Chemistry and Physics, 23, 2765-2787, 10.5194/acp-23-2765-2023, 2023.

Berta, V. Z., Han, S., Osawa, A., Dedrick, J., Maneenoi, N., and Russell, L. M.: Aerosol Quantification Products at Mt. Soledad and Scripps Pier during EPCAPE 2023-24, in, Aerosol Microphysics and Chemical Measurements at Mt. Soledad and Scripps Pier during the Eastern Pacific Cloud Aerosol Precipitation Experiment (EPCAPE) from February 2023 to February 2024, 2025.

Carlton, A., and Turpin, B.: Particle partitioning potential of organic compounds is highest in the Eastern US and driven by anthropogenic water, ATMOSPHERIC CHEMISTRY AND PHYSICS, 13, 10203-10214, 10.5194/acp-13-10203-2013, 2013.

https://doi.org/10.5194/egusphere-2026-4695
Preprint. Discussion started: 24 August 2026

Carlton, A., Christiansen, A., Flesch, M., Hennigan, C., and Sareen, N.: Mulitphase Atmospheric Chemistry in Liquid Water: Impacts and Controllability of Organic Aerosol, ACCOUNTS OF CHEMICAL RESEARCH, 53, 1715-1723, 10.1021/acs.accounts.0c00301, 2020.

Carter, M. L., Flick, R. E., Terrill, E., Beckhaus, E. C., Martin, K., Fey, C. L., Walker, P. W., Largier, J. L., and McGowan, J. A.: Shore Stations Program Data Archive: Current and historical coastal ocean temperature and salinity measurements from California stations, in, UC San Diego Library Digital Collections, 2022.

Chang, R., Slowik, J., Shantz, N., Vlasenko, A., Liggio, J., Sjostedt, S., Leaitch, W., and Abbatt, J.: The hygroscopicity parameter (κ) of ambient organic aerosol at a field site subject to biogenic and anthropogenic influences: relationship to degree of aerosol oxidation, Atmospheric Chemistry and Physics, 10, 5047-5064, 10.5194/acp-10-5047-2010, 2010.

Chen, Q., Sherwen, T., Evans, M., and Alexander, B.: DMS oxidation and sulfur aerosol formation in the marine troposphere: a focus on reactive halogen and multiphase chemistry, ATMOSPHERIC CHEMISTRY AND PHYSICS, 18, 13617-13637, 10.5194/acp-18-13617-2018, 2018.

Cheng, Y., Li, S., Leithead, A., Brickell, P., and Leaitch, W.: Characterizations of cis-pinonic acid and n-fatty acids on fine aerosols in the Lower Fraser Valley during Pacific 2001 Air Quality Study, ATMOSPHERIC ENVIRONMENT, 38, 5789-5800, 10.1016/j.atmosenv.2004.01.051, 2004.

Cheng, Y., Brook, J., Li, S., and Leithead, A.: Seasonal variation in the biogenic secondary organic aerosol tracer cis-pinonic acid: Enhancement due to emissions from regional and local biomass burning, ATMOSPHERIC ENVIRONMENT, 45, 7105-7112, 10.1016/j.atmosenv.2011.09.036, 2011.

Crippa, M., El Haddad, I., Slowik, J. G., DeCarlo, P. F., Mohr, C., Heringa, M. F., Chirico, R., Marchand, N., Sciare, J., Baltensperger, U., and Prevot, A. S. H.: Identification of marine and continental aerosol sources in Paris using high resolution aerosol mass spectrometry, Journal of Geophysical Research-Atmospheres, 118, 1950-1963, 10.1002/jgrd.50151, 2013.

Cubison, M., Ortega, A., Hayes, P., Farmer, D., Day, D., Lechner, M., Brune, W., Apel, E., Diskin, G., Fisher, J., Fuelberg, H., Hecobian, A., Knapp, D., Mikoviny, T., Riemer, D., Sachse, G., Sessions, W., Weber, R., Weinheimer, A., Wisthaler, A., and Jimenez, J.: Effects of aging on organic aerosol from open biomass burning smoke in aircraft and laboratory studies, Atmospheric Chemistry and Physics, 11, 12049-12064, 10.5194/acp-11-12049-2011, 2011.

Day, D. A., Liu, S., Russell, L. M., and Ziemann, P. J.: Organonitrate group concentrations in submicron particles with high nitrate and organic fractions in coastal southern California, Atmospheric Environment, 44, 1970-1979, 10.1016/j.atmosenv.2010.02.045, 2010.

Dedrick, J. L., Osawa, A., Russell, L. M., Miller, M. A., Robinson, L., Chang, R., Williams, A. S., Berta, V. Z., Ravichandran, E., Petters, M., Wheeler, M. J., Han, S., Pelayo, C. N., Maneenoi, N., Lubin, D., Uin, J., Enekwizu, O., Zawadowicz, M., Mayol-Bracero, O., and Twohy, C. H.: Quantitative Estimates of Upwind and On-Site Particle Scavenging and Retrieved Cloud Supersaturations from Urban Coastal Stratocumulus during EPCAPE, Journal of the Atmospheric Sciences, 83, 1061-1082, https://doi.org/10.1175/JAS-D-26-0004.1, 2026.

Devore, J. L., Berk, K. N., and Carlton, M. A.: Modern mathematical statistics with applications, Springer, 2012.

Dobracki, A., Lewis, E., Sedlacek, A. I., Tatro, T., Zawadowicz, M., and Zuidema, P.: Burning conditions and transportation pathways determine biomass-burning aerosol properties in the Ascension Island marine boundary layer, ATMOSPHERIC CHEMISTRY AND PHYSICS, 25, 2333-2363, 10.5194/acp-25-2333-2025, 2025.

Duplissy, J., DeCarlo, P., Dommen, J., Alfarra, M., Metzger, A., Barmpadimos, I., Prevot, A., Weingartner, E., Tritscher, T., Gysel, M., Aiken, A., Jimenez, J., Canagaratna, M., Worsnop, D., Collins, D., Tomlinson, J., and Baltensperger, U.: Relating hygroscopicity and composition of organic aerosol particulate matter, Atmospheric Chemistry and Physics, 11, 1155-1165, 10.5194/acp-11-1155-2011, 2011.

Ervens, B., Turpin, B., and Weber, R.: Secondary organic aerosol formation in cloud droplets and aqueous particles (aqSOA): a review of laboratory, field and model studies, ATMOSPHERIC CHEMISTRY AND PHYSICS, 11, 11069-11102, 10.5194/acp-11-11069-2011, 2011.

Farley, R., Collier, S., Cappa, C., Williams, L., Onasch, T., Russell, L., Kim, H., and Zhang, Q.: Source apportionment of soot particles and aqueous-phase processing of black carbon coatings in an urban environment, ATMOSPHERIC CHEMISTRY AND PHYSICS, 23, 15039-15056, 10.5194/acp-23-15039-2023, 2023.

Farley, R., Gorkowski, K., Lee, J., Benedict, K., Shawon, A., Franco, N., Berta, V., Williams, A., Robinson, L., Chang, R., Dubey, M., Russell, L., and Aiken, A.: Inorganic Nitrate Enhances Cloud Activation of Less Hygroscopic Aerosols at a Coastal Site in California, JOURNAL OF GEOPHYSICAL RESEARCH-ATMOSPHERES, 131, 10.1029/2025JD045943, 2026.

https://doi.org/10.5194/egusphere-2026-4695
Preprint. Discussion started: 24 August 2026

Friedman, B., Link, M., Fulgham, S., Brophy, P., Galang, A., Brune, W., Jathar, S., and Farmer, D.: Primary and Secondary Sources of Gas-Phase Organic Acids from Diesel Exhaust, ENVIRONMENTAL SCIENCE & TECHNOLOGY, 51, 10872-10880, 10.1021/acs.est.7b01169, 2017.

Frossard, A. A., Russell, L. M., Burrows, S. M., Elliott, S. M., Bates, T. S., and Quinn, P. K.: Sources and composition of submicron organic mass in marine aerosol particles, Journal of Geophysical Research-Atmospheres, 119, 12977-13003, 10.1002/2014jd021913, 2014.

Gao, M., Zhou, S., Li, W., Li, F., Teng, X., Li, Y., He, Y., Hang, J., and Wang, X.: Formation and Evolution of Secondary Aerosols at a Mountain Site in Southeastern China: Impacts of Dust Transport and Cloud Processes, JOURNAL OF GEOPHYSICAL RESEARCH-ATMOSPHERES, 130, 10.1029/2025JD044568, 2025.

Ge, X., Zhang, Q., Sun, Y., Ruehl, C., and Setyan, A.: Effect of aqueous-phase processing on aerosol chemistry and size distributions in Fresno, California, during wintertime, Environmental Chemistry, 9, 221-235, 10.1071/EN11168, 2012.

Hakola, H., Arey, J., Aschmann, S., and Atkinson, R.: Product Formation from the Gas-Phase Reactions of OH Radicals and O3 with a Series of Monoterpenes, Journal of Atmospheric Chemistry, 18, 75-102, 10.1007/BF00694375, 1994.

Hall, S., Ullmann, K., Prather, M., Flynn, C., Murray, L., Fiore, A., Correa, G., Strode, S., Steenrod, S., Lamarque, J., Guth, J., Josse, B., Flemming, J., Huijnen, V., Abraham, N., and Archibald, A.: Cloud impacts on photochemistry: building a climatology of photolysis rates from the Atmospheric Tomography mission, ATMOSPHERIC CHEMISTRY AND PHYSICS, 18, 16809-16828, 10.5194/acp-18-16809-2018, 2018.

Hallquist, M., Wenger, J., Baltensperger, U., Rudich, Y., Simpson, D., Claeys, M., Dommen, J., Donahue, N., George, C., Goldstein, A., Hamilton, J., Herrmann, H., Hoffmann, T., Iinuma, Y., Jang, M., Jenkin, M., Jimenez, J., Kiendler-Scharr, A., Maenhaut, W., McFiggans, G., Mentel, T., Monod, A., Prévôt, A., Seinfeld, J., Surratt, J., Szmigielski, R., and Wildt, J.: The formation, properties and impact of secondary organic aerosol: current and emerging issues, Atmospheric Chemistry and Physics, 9, 5155-5236, 10.5194/acp-9-5155-2009, 2009.

Han, S., S., W. A., M., R. L., Z., B. V., L., D. J., Christian, P., Nattamon, M., Atsushi, O., Israel, S., Damao, Z., A., Z. M., and Sedlacek Arthur J., I.: Nearby Sites Show Similar Upwind Sources and Differing Semivolatile Concentrations in Coastal Aerosol Particles, ACS ES\&T Air, 2, 2824-2837, 10.1021/acsestair.5c00191, 2025.

Hawkins, L. N., and Russell, L. M.: Oxidation of ketone groups in transported biomass burning aerosol from the 2008 Northern California Lightning Series fires, Atmospheric Environment, 44, 4142-4154, 10.1016/j.atmosenv.2010.07.036, 2010.

He, L., Lin, Y., Huang, X., Guo, S., Xue, L., Su, Q., Hu, M., Luan, S., and Zhang, Y.: Characterization of high-resolution aerosol mass spectra of primary organic aerosol emissions from Chinese cooking and biomass burning, Atmospheric Chemistry and Physics, 10, 11535-11543, 10.5194/acp-10-11535-2010, 2010.

Heutte, B., Angot, H., Chen, G., Pernov, J., El Haddad, I., Dada, L., Daellenbach, K., Beck, I., Bergner, N., Bucci, S., Creamean, J., Kulmala, M., Laurila, T., Petaja, T., Pratt, K., Prevot, A., Quelever, L., Zieger, P., Jokinen, T., and Schmale, J.: Sources and Composition of Organic Aerosols in the Central Arctic during Spring and Summer, Environmental Science & Technology, 59, 21924-21940, 10.1021/acs.est.5c09788, 2025.

Hoffmann, T., Bandur, R., Marggraf, U., and Linscheid, M.: Molecular composition of organic aerosols formed in the α-pinene/O3 reaction: Implications for new particle formation processes, JOURNAL OF GEOPHYSICAL RESEARCH-ATMOSPHERES, 103, 25569-25578, 10.1029/98JD01816, 1998.

Hoppel, W., Fitzgerald, J., Frick, G., Larson, R., and Mack, E.: Aerosol Size Distributions and Optical-Properties Found in the Marine Boundary-Layer over the Atlantic-Ocean, Journal of Geophysical Research-Atmospheres, 95, 3659-3686, 10.1029/JD095iD04p03659, 1990.

Huang, D., Kong, L., Gao, J., Lou, S., Qiao, L., Zhou, M., Ma, Y., Zhu, S., Wang, H., Chen, S., Zeng, L., and Huang, C.: Insights into the formation and properties of secondary organic aerosol at a background site in Yangtze River Delta region of China: Aqueous-phase processing vs. photochemical oxidation, Atmospheric Environment, 239, 10.1016/j.atmosenv.2020.117716, 2020.

Huang, S., Poulain, L., van Pinxteren, D., van Pinxteren, M., Wu, Z., Herrmann, H., and Wiedensohler, A.: Latitudinal and Seasonal Distribution of Particulate MSA over the Atlantic using a Validated Quantification Method with HR-ToF-AMS, Environmental Science & Technology, 51, 418-426, 10.1021/acs.est.6b03186, 2017.

Imanova, A., Rozanov, E., Smyshlyaev, S., Zubov, V., and Egorova, T.: Investigation of the Influence of Atmospheric Scattering on Photolysis Rates Using the Cloud-J Module, ATMOSPHERE, 16, 10.3390/atmos16010058, 2025.

https://doi.org/10.5194/egusphere-2026-4695
Preprint. Discussion started: 24 August 2026

James, M., Moschos, V., McRee, M., Fiddler, M., Turpin, B., Surratt, J., and Bililign, S.: Real-time chemical characterization of primary and aged biomass burning aerosols derived from sub-Saharan African biomass fuels in smoldering fires, Environmental Science-Atmospheres, 4, 1382-1397, 10.1039/d4ea00110a, 2024.

Jayaraman, A., Lubin, D., Ramachandran, S., Ramanathan, V., Woodbridge, E., Collins, W., and Zalpuri, K.: Direct observations of aerosol radiative forcing over the tropical Indian Ocean during the January-February 1996 pre-INDOEX cruise, JOURNAL OF GEOPHYSICAL RESEARCH-ATMOSPHERES, 103, 13827-13836, 10.1029/98JD00559, 1998.

Jiang, H., Deng, Y., Huo, Y., Wang, F., Chen, Y., and Guo, H.: Measurement report: Molecular insights into organic aerosol sources and formation at a regional background site in South China, Atmospheric Chemistry and Physics, 25, 13711-13727, 10.5194/acp-25-13711-2025, 2025.

Jimenez, J., Canagaratna, M., Donahue, N., Prevot, A., Zhang, Q., Kroll, J., DeCarlo, P., Allan, J., Coe, H., Ng, N., Aiken, A., Docherty, K., Ulbrich, I., Grieshop, A., Robinson, A., Duplissy, J., Smith, J., Wilson, K., Lanz, V., Hueglin, C., Sun, Y., Tian, J., Laaksonen, A., Raatikainen, T., Rautiainen, J., Vaattovaara, P., Ehn, M., Kulmala, M., Tomlinson, J., Collins, D., Cubison, M., Dunlea, E., Huffman, J., Onasch, T., Alfarra, M., Williams, P., Bower, K., Kondo, Y., Schneider, J., Drewnick, F., Borrmann, S., Weimer, S., Demerjian, K., Salcedo, D., Cottrell, L., Griffin, R., Takami, A., Miyoshi, T., Hatakeyama, S., Shimono, A., Sun, J., Zhang, Y., Dzepina, K., Kimmel, J., Sueper, D., Jayne, J., Herndon, S., Trimborn, A., Williams, L., Wood, E., Middlebrook, A., Kolb, C., Baltensperger, U., and Worsnop, D.: Evolution of Organic Aerosols in the Atmosphere, Science, 326, 1525-1529, 10.1126/science.1180353, 2009.

Kapp, A., and Smith, J. N.: Particle composition measurements for ultrafine particles collected at the EPCAPE Mount Soledad site from 2023-04-27 to 2023-06-13 using a Thermal Desorption Chemical Ionization Mass Spectrometer, in, Atmospheric Radiation Measurement (ARM) User Facility, U.S. Department of Energy, 2025.

Kavouras, I., Mihalopoulos, N., and Stephanou, E.: Formation of atmospheric particles from organic acids produced by forests, NATURE, 395, 683-686, 10.1038/27179, 1998.

Kavouras, I., Mihalopoulos, N., and Stephanou, E.: Secondary organic aerosol formation vs primary organic aerosol emission: In situ evidence for the chemical coupling between monoterpene acidic photooxidation products and new particle formation over forests, ENVIRONMENTAL SCIENCE & TECHNOLOGY, 33, 1028-1037, 10.1021/es9807035, 1999.

Kolodziejczyk, A., Pyrcz, P., Pobudkowska, A., Blaziak, K., and Szmigielski, R.: Physicochemical Properties of Pinic, Pinonic, Norpinic, and Norpinonic Acids as Relevant α-Pinene Oxidation Products, JOURNAL OF PHYSICAL CHEMISTRY B, 123, 8261-8267, 10.1021/acs.jpcb.9b05211, 2019.

Kroll, J., and Seinfeld, J.: Chemistry of secondary organic aerosol: Formation and evolution of low-volatility organics in the atmosphere, ATMOSPHERIC ENVIRONMENT, 42, 3593-3624, 10.1016/j.atmosenv.2008.01.003, 2008.

Lambe, A., Onasch, T., Massoli, P., Croasdale, D., Wright, J., Ahern, A., Williams, L., Worsnop, D., Brune, W., and Davidovits, P.: Laboratory studies of the chemical composition and cloud condensation nuclei (CCN) activity of secondary organic aerosol (SOA) and oxidized primary organic aerosol (OPOA), ATMOSPHERIC CHEMISTRY AND PHYSICS, 11, 8913-8928, 10.5194/acp-11-8913-2011, 2011.

Li, J., Cao, L., Gao, W., He, L., Yan, Y., He, Y., Pan, Y., Ji, D., Liu, Z., and Wang, Y.: Seasonal variations in the highly time-resolved aerosol composition, sources and chemical processes of background submicron particles in the North China Plain, ATMOSPHERIC CHEMISTRY AND PHYSICS, 21, 4521-4539, 10.5194/acp-21-4521-2021, 2021.

Liggio, J., Wentzell, J., and Wheeler, M.: Online Gas-phase Organic and Inorganic Chemical Composition at Mt. Soledad during EPCAPE 2023-24, in, UC San Diego Library Digital Collections, Aerosol Microphysics and Chemical Measurements at Mt. Soledad and Scripps Pier during the Eastern Pacific Cloud Aerosol Precipitation Experiment (EPCAPE) from February 2023 to February 2024, 2025.

Lim, Y., Tan, Y., Perri, M., Seitzinger, S., and Turpin, B.: Aqueous chemistry and its role in secondary organic aerosol (SOA) formation, ATMOSPHERIC CHEMISTRY AND PHYSICS, 10, 10521-10539, 10.5194/acp-10-10521-2010, 2010.

Liu, S., Day, D. A., Shields, J. E., and Russell, L. M.: Ozone-driven daytime formation of secondary organic aerosol containing carboxylic acid groups and alkane groups, Atmospheric Chemistry and Physics, 11, 8321-8341, 10.5194/acp-11-8321-2011, 2011.

Liu, Y., Monod , A., Tritscher , T., Praplan, A. P., P.F., D., B., T.-R., E., Q., N., M., J., D., and U., B.: Aqueous phase processing of secondary organic aerosol from isoprene photooxidation, in, Atmospheric Chemistry and Physics, 5879–5895, 2012.

Lubin, D., and Simpson, A. S.: Measurement of surface radiation fluxes and cloud optical properties during the 1994 Arctic Ocean Section, Journal of Geophysical Research: Atmospheres, 102, 4275-4286, https://doi.org/10.1029/96JD03215, 1997.

https://doi.org/10.5194/egusphere-2026-4695
Preprint. Discussion started: 24 August 2026

Maneenoi, N., Russell, L. M., Han, S., Dedrick, J. L., Williams, A. S., Berta, V. Z., Pelayo, C., Zawadowicz, M. A., Sedlacek, A. J., 3rd, Silber, I., Thieman, M., Painemal, D., and Shen, S. S. P.: Photochemical and Cloud and Aerosol Aqueous Contributions to Regionally-Emitted Shipping and Biogenic Non-Sea-Salt Sulfate Aerosol in Coastal California, ACS EST Air, 2, 648-664, 10.1021/acsestair.4c00352, 2025.

Maria, S. F., Russell, L. M., Turpin, B. J., Porcja, R. J., Campos, T. L., Weber, R. J., and Huebert, B. J.: Source signatures of carbon monoxide and organic functional groups in Asian Pacific Regional Aerosol Characterization Experiment (ACE-Asia) submicron aerosol types, Journal of Geophysical Research-Atmospheres, 108, 14, 10.1029/2003jd003703, 2003.

Maria, S. F., Russell, L. M., Gilles, M. K., and Myneni, S. C. B.: Organic aerosol growth mechanisms and their climate-forcing implications, Science, 306, 1921-1924, 10.1126/science.1103491, 2004.

Mattila, J., Brophy, P., Kirkland, J., Hall, S., Ullmann, K., Fischer, E., Brown, S., McDuffie, E., Tevlin, A., and Farmer, D.: Tropospheric sources and sinks of gas-phase acids in the Colorado Front Range, ATMOSPHERIC CHEMISTRY AND PHYSICS, 18, 12315-12327, 10.5194/acp-18-12315-2018, 2018.

McNeill, V.: Aqueous Organic Chemistry in the Atmosphere: Sources and Chemical Processing of Organic Aerosols, ENVIRONMENTAL SCIENCE & TECHNOLOGY, 49, 1237-1244, 10.1021/es5043707, 2015.

Mohr, C., DeCarlo, P., Heringa, M., Chirico, R., Slowik, J., Richter, R., Reche, C., Alastuey, A., Querol, X., Seco, R., Peñuelas, J., Jiménez, J., Crippa, M., Zimmermann, R., Baltensperger, U., and Prévôt, A.: Identification and quantification of organic aerosol from cooking and other sources in Barcelona using aerosol mass spectrometer data, Atmospheric Chemistry and Physics, 12, 1649-1665, 10.5194/acp-12-1649-2012, 2012.

Nojgaard, J., Peker, L., Pernov, J., Johnson, M., Bossi, R., Massling, A., Lange, R., Nielsen, I., Prevot, A., Eriksson, A., Canonaco, F., and Skov, H.: A local marine source of atmospheric particles in the High Arctic, Atmospheric Environment, 285, 10.1016/j.atmosenv.2022.119241, 2022.

O'Dowd, C., Aalto, P., Hämeri, K., Kulmala, M., and Hoffmann, T.: Aerosol formation -: Atmospheric particles from organic vapours, NATURE, 416, 497-498, 10.1038/416497a, 2002.

Pelayo, C., Maneenoi, N., Berta, V., and Russell, L. M.: Filter Organic and Elemental Composition of Submicron Aerosol Particles and Particle Number Concentration at Mt. Soledad during EPCAPE 2023-24, in, UC San Diego Library Digital Collections, Aerosol Microphysics and Chemical Measurements at Mt. Soledad and Scripps Pier during the Eastern Pacific Cloud Aerosol Precipitation Experiment (EPCAPE) from February 2023 to February 2024, 2025.

Qin, Y., Li, Y., Wang, H., Lee, B., Huang, D., and Chan, C.: Particulate matter (PM) episodes at a suburban site in Hong Kong: evolution of PM characteristics and role of photochemistry in secondary aerosol formation, Atmospheric Chemistry and Physics, 16, 14131-14145, 10.5194/acp-16-14131-2016, 2016.

Quinn, P. K., Bates, T. S., Coffman, D. J., Upchurch, L., Johnson, J. E., Moore, R., Ziemba, L., Bell, T. G., Saltzman, E. S., Graff, J., and Behrenfeld, M. J.: Seasonal Variations in Western North Atlantic Remote Marine Aerosol Properties, Journal of Geophysical Research-Atmospheres, 124, 14240-14261, 10.1029/2019jd031740, 2019.

Roustaei, N.: Application and interpretation of linear-regression analysis, Med Hypothesis Discov Innov Ophthalmol, 13, 151-159, 10.51329/mehdiophthal1506, 2024.

Russell, L. M., Han, S., Williams, A. S., Berta, V., Dedrick, J. L., Pelayo, C., Maneenoi, N., Petters, M., Ravichandran, E., Chang, R., Kapp, A., Smith, J. N., Wheeler, M., Wentzell, J., and Liggio, J.: Aerosol Microphysics and Chemical Measurements at Mt. Soledad and Scripps Pier during the Eastern Pacific Cloud Aerosol Precipitation Experiment (EPCAPE) from February 2023 to February 2024, in, UC San Diego Library Digital Collections, 2023.

Saliba, G., Chen, C. L., Lewis, S., Russell, L. M., Rivellini, L. H., Lee, A. K. Y., Quinn, P. K., Bates, T. S., Haentjens, N., Boss, E. S., Karp-Boss, L., Baetge, N., Carlson, C. A., and Behrenfeld, M. J.: Factors driving the seasonal and hourly variability of sea-spray aerosol number in the North Atlantic, Proceedings of the National Academy of Sciences of the United States of America, 116, 20309-20314, 10.1073/pnas.1907574116, 2019.

Saliba, G., Chen, C. L., Lewis, S., Russell, L. M., Quinn, P. K., Bates, T. S., Bell, T. G., Lawler, M. J., Saltzman, E. S., Sanchez, K. J., Moore, R., Shook, M., Rivellini, L. H., Lee, A., Baetge, N., Carlson, C. A., and Behrenfeld, M. J.: Seasonal Differences and Variability of Concentrations, Chemical Composition, and Cloud Condensation Nuclei of Marine Aerosol Over the North Atlantic, Journal of Geophysical Research-Atmospheres, 125, 10.1029/2020JD033145, 2020.

Sengupta, M., Habte, A., Andreas, A., Reda, I., Jaker, S., Xie, Y., Yang, J., Gotseff, P., Kutchenreiter, M., and Shi, Y.: Sky Radiometers on Stand for Downwelling Radiation (SKYRAD60S), 2023-02-15 to 2024-02-14, ARM Mobile Facility (EPC),

https://doi.org/10.5194/egusphere-2026-4695
Preprint. Discussion started: 24 August 2026

La Jolla, CA; AMF1 (main site for EPCAPE on Scripps Pier) (M1), in, Atmospheric Radiation Measurement (ARM) User Facility, 2023.

Silber, I., Comstock, J., Kieburtz, M., and Russell, L.: ARMTRAJ: a set of multipurpose trajectory datasets augmenting the Atmospheric Radiation Measurement (ARM) user facility measurements, EARTH SYSTEM SCIENCE DATA, 17, 29-42, 10.5194/essd-17-29-2025, 2025.

Song, J., Saathoff, H., Jiang, F., Gao, L., Zhang, H., and Leisner, T.: Sources of organic gases and aerosol particles and their roles in nighttime particle growth at a rural forested site in southwest Germany, Atmospheric Chemistry and Physics, 24, 6699-6717, 10.5194/acp-24-6699-2024, 2024.

Sonntag, D., Bailey, C., Fulper, C., and Baldauf, R.: Contribution of Lubricating Oil to Particulate Matter Emissions from Light-Duty Gasoline Vehicles in Kansas City, ENVIRONMENTAL SCIENCE & TECHNOLOGY, 46, 4191-4199, 10.1021/es203747f, 2012.

Takahama, S., Johnson, A., and Russell, L. M.: Quantification of Carboxylic and Carbonyl Functional Groups in Organic Aerosol Infrared Absorbance Spectra, Aerosol Science and Technology, 47, 310-325, 10.1080/02786826.2012.752065, 2013.

Tiitta, P., Leskinen, A., Hao, L., Yli-Pirilä, P., Kortelainen, M., Grigonyte, J., Tissari, J., Lamberg, H., Hartikainen, A., Kuuspalo, K., Kortelainen, A., Virtanen, A., Lehtinen, K., Komppula, M., Pieber, S., Prévôt, A., Onasch, T., Worsnop, D., Czech, H., Zimmermann, R., Jokiniemi, J., and Sippula, O.: Transformation of logwood combustion emissions in a smog chamber: formation of secondary organic aerosol and changes in the primary organic aerosol upon daytime and nighttime aging, Atmospheric Chemistry and Physics, 16, 13251-13269, 10.5194/acp-16-13251-2016, 2016.

Tong, Y., Qi, L., Stefenelli, G., Wang, D., Canonaco, F., Baltensperger, U., Prevot, A., and Slowik, J.: Quantification of primary and secondary organic aerosol sources by combined factor analysis of extractive electrospray ionisation and aerosol mass spectrometer measurements (EESI-TOF and AMS), ATMOSPHERIC MEASUREMENT TECHNIQUES, 15, 7265-7291, 10.5194/amt-15-7265-2022, 2022.

Ulbrich, I. M., Canagaratna, M. R., Zhang, Q., Worsnop, D. R., and Jimenez, J. L.: Interpretation of organic components from Positive Matrix Factorization of aerosol mass spectrometric data, Atmospheric Chemistry and Physics, 9, 2891-2918, 10.5194/acp-9-2891-2009, 2009.

Usher, C., Michel, A., and Grassian, V.: Reactions on mineral dust, CHEMICAL REVIEWS, 103, 4883-4939, 10.1021/cr020657y, 2003.

Veres, P., Roberts, J., Cochran, A., Gilman, J., Kuster, W., Holloway, J., Graus, M., Flynn, J., Lefer, B., Warneke, C., and de Gouw, J.: Evidence of rapid production of organic acids in an urban air mass, Geophysical Research Letters, 38, 10.1029/2011GL048420, 2011.

Wan, Z., Song, K., Zhu, W., Yu, Y., Wang, H., Shen, R., Tan, R., Lv, D., Gong, Y., Yu, X., Chen, S., Zeng, L., Lou, S., Yu, Y., and Guo, S.: A Closure Study of Secondary Organic Aerosol Estimation at an Urban Site of Yangtze River Delta, China, ATMOSPHERE, 13, 10.3390/atmos13101679, 2022.

Williams, A. S., Russell, L. M., Han, S., Berta, V. Z., Dedrick, J. L., Campos, T., Robinson, L. T., Chang, R. Y.-W., Farley , R. N., Aiken, A. C., Twohy, C. H., Wheeler, M. J., Wentzell , J. J. B., and Liggio, J.: Cloud Property, Aerosol Activation, and Aqueous Reaction Effects on Nitrate in Coastal Clouds, in review, 2026.

Xiao, Y., Hu, M., Zong, T., Wu, Z., Tan, T., Zhang, Z., Fang, X., Chen, S., and Guo, S.: Insights into aqueous-phase and photochemical formation of secondary organic aerosol in the winter of Beijing, ATMOSPHERIC ENVIRONMENT, 259, 10.1016/j.atmosenv.2021.118535, 2021.

Xu, W., Han, T., Du, W., Wang, Q., Chen, C., Zhao, J., Zhang, Y., Li, J., Fu, P., Wang, Z., Worsnop, D., and Sun, Y.: Effects of Aqueous-Phase and Photochemical Processing on Secondary Organic Aerosol Formation and Evolution in Beijing, China, Environmental Science and Technology, 51, 762-770, 10.1021/acs.est.6b04498, 2017.

Xu, W., Ovadnevaite, J., Fossum, K., Huang, R., Huang, D., Zhong, H., Gu, Y., Lin, C., Huang, C., O'Dowd, C., and Ceburnis, D.: Condensation of organic-inorganic vapours governs the production of ultrafine secondary marine cloud nuclei, COMMUNICATIONS EARTH & ENVIRONMENT, 5, 10.1038/s43247-024-01519-z, 2024.

Yao, D., Guo, H., Lyu, X., Lu, H., and Huo, Y.: Secondary organic aerosol formation at an urban background site on the coastline of South China: Precursors and aging processes, ENVIRONMENTAL POLLUTION, 309, 10.1016/j.envpol.2022.119778, 2022.

https://doi.org/10.5194/egusphere-2026-4695
Preprint. Discussion started: 24 August 2026

Zawadowicz, M., Howie, J., Shilling, J., and Levin, M.: ACSM, corrected for composition-dependent collection efficiency (ACSMCDCE), 2023-02-15 to 2024-02-15, ARM Mobile Facility (EPC), La Jolla, CA; AMF1 (main site for EPCAPE on Scripps Pier) (M1), in, Atmospheric Radiation Measurement (ARM) User Facility, 2023.

Zhan, B., Zhong, H., Chen, H., Chen, Y., Li, X., Wang, L., Wang, X., Mu, Y., Huang, R., George, C., and Chen, J.: The roles of aqueous-phase chemistry and photochemical oxidation in oxygenated organic aerosols formation, Atmospheric Environment, 266, 10.1016/j.atmosenv.2021.118738, 2021.

Zhang, C., Wang, Y., Liu, J., Chen, T., Huang, W., Liu, Z., Chu, B., Ma, Q., and He, H.: Insight into wet scavenging effects on sulfur and nitrogen containing organic compounds in urban Beijing, NPJ CLIMATE AND ATMOSPHERIC SCIENCE, 7, 10.1038/s41612-024-00756-5, 2024.

Zhang, Q., Jimenez, J., Canagaratna, M., Allan, J., Coe, H., Ulbrich, I., Alfarra, M., Takami, A., Middlebrook, A., Sun, Y., Dzepina, K., Dunlea, E., Docherty, K., DeCarlo, P., Salcedo, D., Onasch, T., Jayne, J., Miyoshi, T., Shimono, A., Hatakeyama, S., Takegawa, N., Kondo, Y., Schneider, J., Drewnick, F., Borrmann, S., Weimer, S., Demerjian, K., Williams, P., Bower, K., Bahreini, R., Cottrell, L., Griffin, R., Rautiainen, J., Sun, J., Zhang, Y., and Worsnop, D.: Ubiquity and dominance of oxygenated species in organic aerosols in anthropogenically-influenced Northern Hemisphere midlatitudes, GEOPHYSICAL RESEARCH LETTERS, 34, 10.1029/2007GL029979, 2007.

Zorn, S., Drewnick, F., Schott, M., Hoffmann, T., and Borrmann, S.: Characterization of the South Atlantic marine boundary layer aerosol using an aerodyne aerosol mass spectrometer, Atmospheric Chemistry and Physics, 8, 4711-4728, 10.5194/acp-8-4711-2008, 2008.

https://doi.org/10.5194/egusphere-2026-4695
Preprint. Discussion started: 24 August 2026

Tables

https://doi.org/10.5194/egusphere-2026-4695
Preprint. Discussion started: 24 August 2026

Table 1: Multivariate linear regression (MLR) results showing normalized absolute and relative predictor contributions to predicted PMF factor mass concentrations (SR-OOA, MO-OOA, LO-OOA, C-OOA) and bulk O/C at Mt. Soledad. Predictor variables include ozone (O_3), upwind cloud volume fraction (UCVF), relative humidity (RH), refractory black carbon (rBC), and local cloud fraction (LCF). Values are reported as $m_i\bar{X}_{norm,i}$ with relative contributions (%) given in parentheses, calculated as the fractional contribution of each predictor to the sum of absolute contributions. Results are shown for annual, seasonal, and CNW trajectory subsets. Model performance is evaluated using uncentered coefficient of determination (R^2) and root mean square error (RMSE).

Predicted Variable	Ozone	UCVF	RH	rBC	LCF	R^2	RSME
O/C							
Annual	**0.36 (38%)**	0.19 (19%)	**0.37 (39%)**	0.01 (2%)	-0.02 (-2%)	0.97	0.16
Winter	**0.45 (58%)**	0.08 (11%)	0.20 (26%)	0.02 (3%)	0.02 (3%)	0.97	0.13
Spring	0.17 (15%)	0.27 (24%)	**0.60 (52%)**	-0.01 (0%)	-0.11 (-9%)	0.97	0.17
Summer	**0.34 (33%)**	0.11 (11%)	**0.58 (56%)**	0.00 (0%)	-0.01 (-1%)	0.97	0.18
Fall	**0.58 (70%)**	0.05 (7%)	0.15 (18%)	0.00 (0%)	0.04 (5%)	0.97	0.14
Annual-CNW	**0.30 (28%)**	0.20 (18%)	**0.50 (47%)**	0.01 (1%)	-0.05 (-5%)	0.98	0.15
SR-OOA							
Annual	-0.03 (-11%)	**0.21 (70%)**	0.04 (14%)	0.00 (0%)	-0.01 (-5%)	0.64	0.18
Winter	**0.07 (55%)**	0.02 (17%)	-0.02 (-12%)	-0.01 (-7%)	0.01 (10%)	0.55	0.08
Spring	0.04 (12%)	**0.15 (45%)**	0.08 (24%)	-0.01 (-2%)	-0.05 (-16%)	0.75	0.13
Summer	0.07 (16%)	**0.30 (68%)**	0.03 (6%)	-0.03 (-6%)	-0.02 (-4%)	0.74	0.22
Fall	-0.02 (-15%)	**0.07 (61%)**	0.01 (9%)	-0.01 (-5%)	0.01 (11%)	0.41	0.11
Annual-CNW	-0.02 (-5%)	**0.24 (68%)**	0.06 (16%)	0.00 (1%)	-0.04 (-11%)	0.66	0.19
MO-OOA							
Annual	0.15 (14%)	0.29 (26%)	0.34 (31%)	0.16 (15%)	-0.15 (-14%)	0.27	1.37
Winter	**0.23 (44%)**	0.08 (16%)	-0.12 (-24%)	0.04 (8%)	-0.04 (-9%)	0.65	0.17
Spring	0.14 (23%)	**0.30 (48%)**	-0.17 (-26%)	0.01 (2%)	0.01 (2%)	0.71	0.21
Summer	**3.03 (46%)**	-2.30 (-35%)	0.89 (14%)	0.29 (4%)	-0.05 (-1%)	0.62	1.76
Fall	**0.43 (77%)**	0.07 (13%)	0.00 (1%)	0.04 (7%)	0.01 (2%)	0.65	0.43
Annual-CNW	**0.37 (32%)**	-0.02 (-2%)	0.22 (19%)	**0.44 (38%)**	-0.09 (-8%)	0.33	1.52
LO-OOA							
Annual	**0.52 (64%)**	-0.10 (-13%)	-0.16 (-19%)	0.01 (2%)	-0.03 (-3%)	0.37	0.39
Winter	**0.37 (38%)**	**0.31 (32%)**	-0.24 (-24%)	0.02 (2%)	-0.05 (-5%)	0.39	0.58
Spring	**0.51 (57%)**	-0.05 (-6%)	-0.22 (-25%)	0.08 (8%)	-0.04 (-5%)	0.56	0.36
Summer	**0.17 (36%)**	-0.17 (-36%)	0.07 (15%)	0.06 (12%)	0.00 (0%)	0.40	0.20
Fall	**0.22 (55%)**	-0.04 (-10%)	0.05 (13%)	0.03 (8%)	-0.05 (-13%)	0.51	0.23
Annual-CNW	**0.45 (56%)**	-0.12 (-15%)	-0.18 (-23%)	0.04 (5%)	0.02 (2%)	0.42	0.27
C-OOA							
Annual	0.01 (2%)	-0.02 (-2%)	**0.45 (53%)**	**0.23 (26%)**	-0.14 (-17%)	0.45	0.70
Winter	0.02 (13%)	0.03 (16%)	-0.01 (-5%)	**0.08 (49%)**	-0.03 (-17%)	0.62	0.15
Spring	-0.03 (-12%)	**0.07 (25%)**	**0.11 (37%)**	0.01 (3%)	-0.07 (-23%)	0.34	0.14
Summer	**1.19 (37%)**	-1.06 (-33%)	0.58 (18%)	0.33 (10%)	0.02 (1%)	0.68	0.84
Fall	**0.58 (43%)**	-0.16 (-12%)	0.28 (21%)	0.25 (19%)	-0.08 (-6%)	0.77	0.53
Annual-CNW	-0.02 (-2%)	-0.13 (-15%)	**0.39 (42%)**	**0.32 (35%)**	-0.05 (-6%)	0.46	0.71

https://doi.org/10.5194/egusphere-2026-4695
Preprint. Discussion started: 24 August 2026

Figures

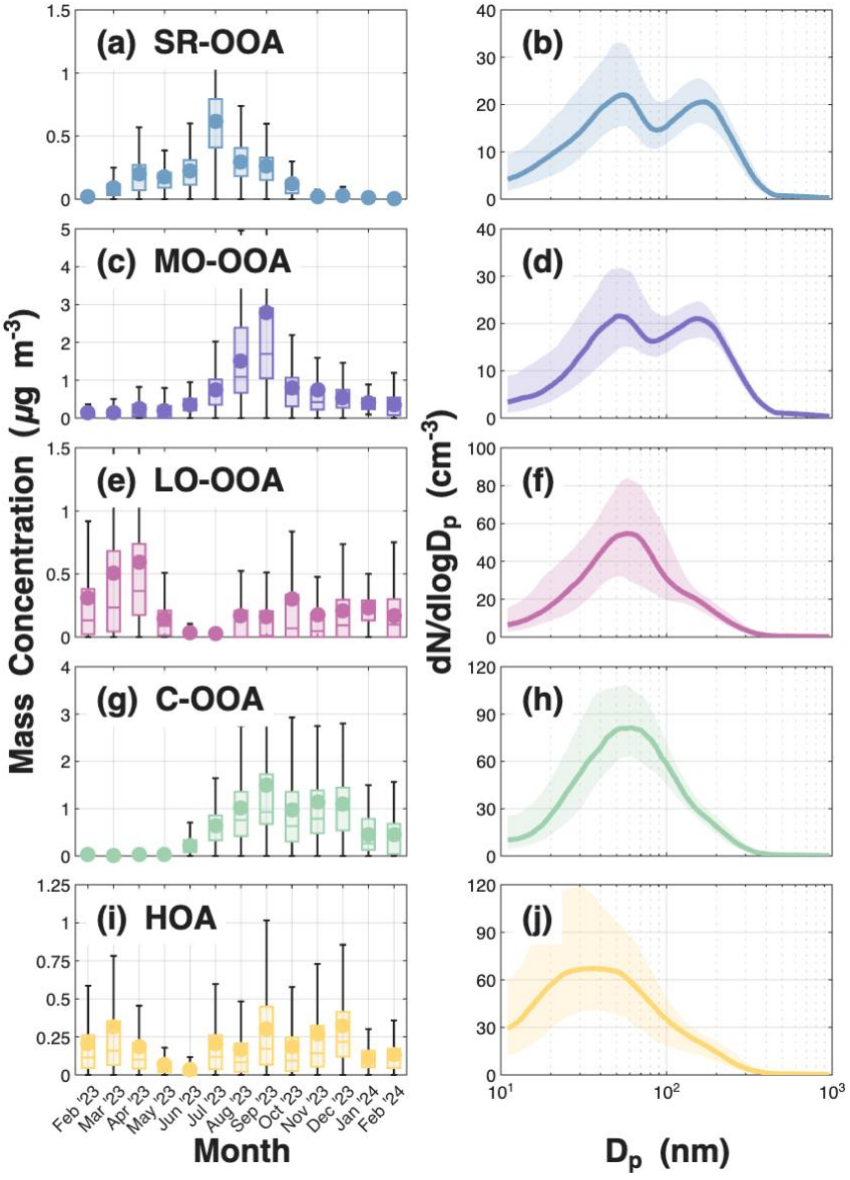

Figure 1: Monthly average mass concentrations (μg m^{-3}) of AMS NR organic PMF factors at Mt. Soledad, including (a) SR-OOA, (c) MO-OOA, (e) LO-OOA, (g) C-OOA, and (i) HOA, respectively. Colored dots represent the monthly means. The boxes indicate the interquartile range (IQR; 25th–75th percentile), with the middle line marking the median, the top edge representing the 75th percentile, and the bottom edge representing the 25th percentile. The whiskers extend to the maximum and minimum non-outlier values. The median particle number size distributions during periods when PMF factor mass concentrations exceeded their 80th percentile and were unique to that factor (i.e., not simultaneously above the 80th percentile for the other PMF factors) are shown (b,d,f,h,j). Shaded regions represent the IQR. Mass concentrations exclude times with particle number concentrations exceeding 8000 cm^{-3}.

https://doi.org/10.5194/egusphere-2026-4695
Preprint. Discussion started: 24 August 2026

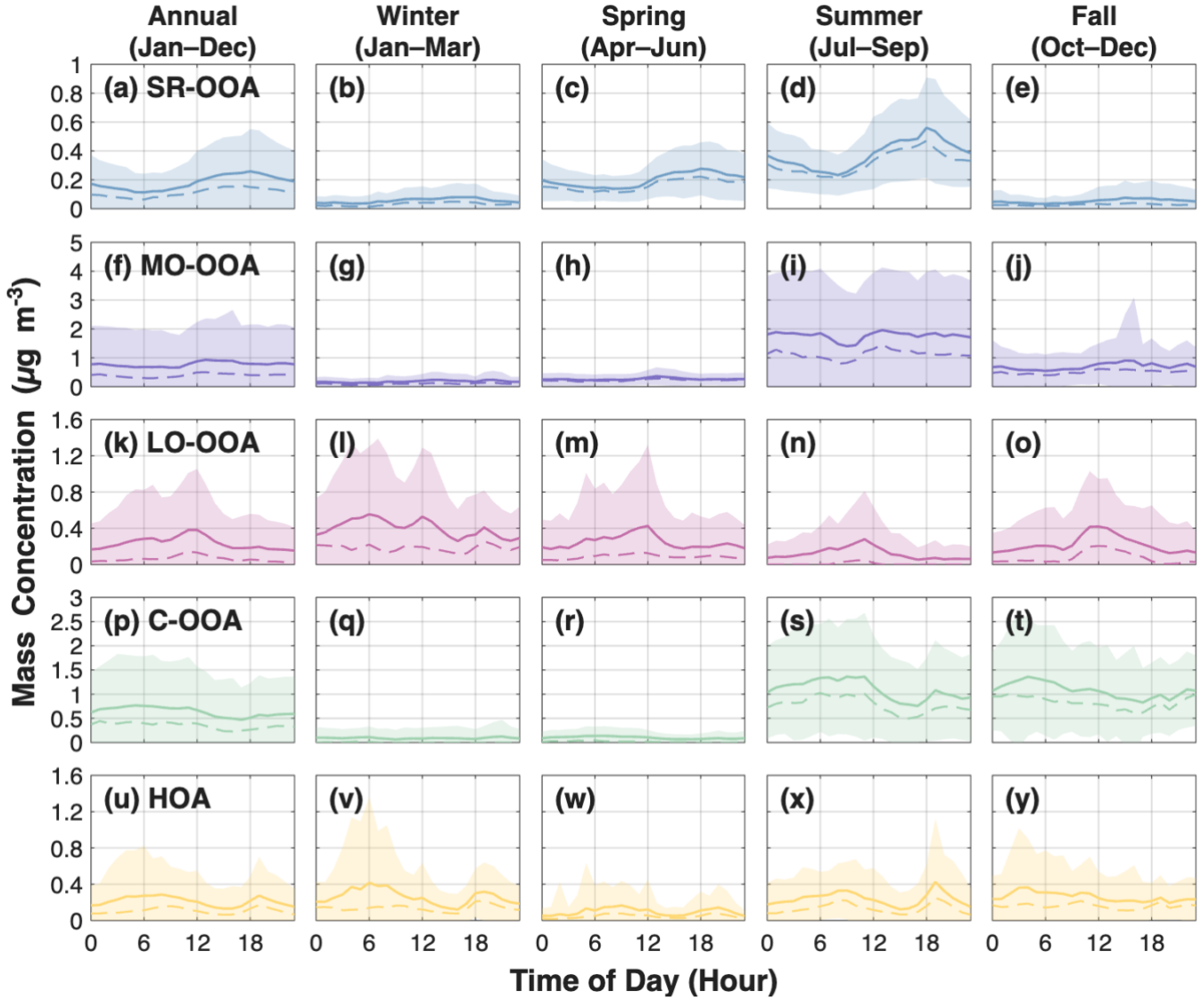

Figure 2: Diurnal patterns in AMS NR organic PMF factors at Mt. Soledad in local time (PT) for (a–e) SR-OOA, (f–j) MO-OOA, (k–o) LO-OOA, (p–t) C-OOA, and (u–y) HOA. Columns correspond to annual conditions, winter, spring, summer, and fall from left to right. The shaded area represents the standard deviation, the solid line represents the mean, and the dashed line represents the median. Mass concentrations exclude times with particle number concentrations exceeding 8000 cm^{-3}.

https://doi.org/10.5194/egusphere-2026-4695
Preprint. Discussion started: 24 August 2026

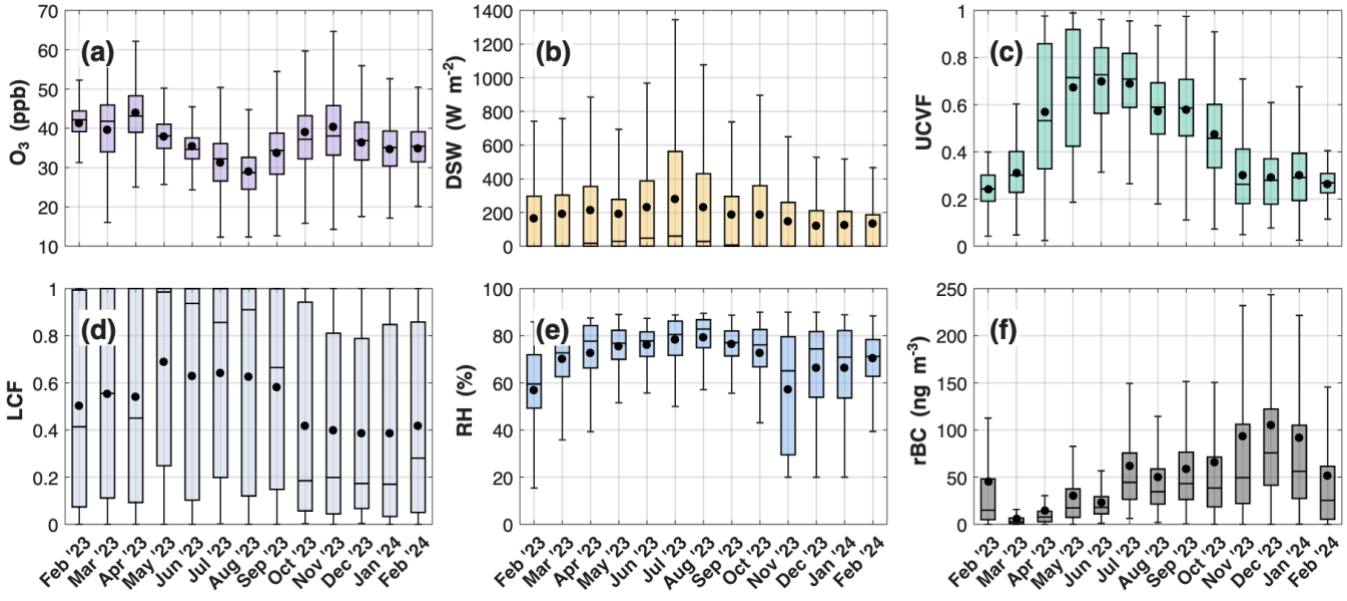

Figure 3: Box plots of monthly average values of (a) O_3, (b) DSW, (c) UCVF, (d) LCF, (e) RH, and (f) rBC at Mt. Soledad. The black dots represent the monthly means. O_3 and rBC exclude times with particle number concentrations exceeding 8000 cm^{-3}. The boxes indicate the interquartile range (IQR), with the middle line marking the median, the top edge representing the 75th percentile, and the bottom edge representing the 25th percentile. The whiskers extend to the maximum and minimum non-outlier values.

https://doi.org/10.5194/egusphere-2026-4695
Preprint. Discussion started: 24 August 2026

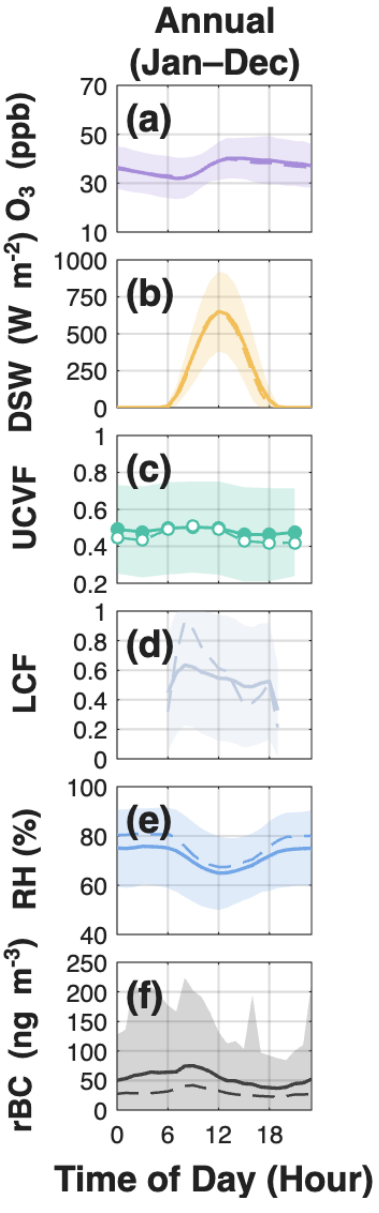

Figure 4: Annual diurnal patterns of (a) O_3, (b) DSW, (c) UCVF, (d) LCF, (e) RH, and (f) rBC at Mt. Soledad for all back-trajectories. O3, DSW, LCF, RH, and rBC are shown in local time (PT), while UCVF is shown in UTC corresponding to its original 3-hour temporal resolution. O_3 and rBC exclude times with particle number concentrations exceeding 8000 cm^{-3}. The shaded area represents the standard deviation, the solid line represents the average, and the dashed line represents the median. For UCVF, filled markers indicate mean values and open markers indicate median values.

https://doi.org/10.5194/egusphere-2026-4695
Preprint. Discussion started: 24 August 2026

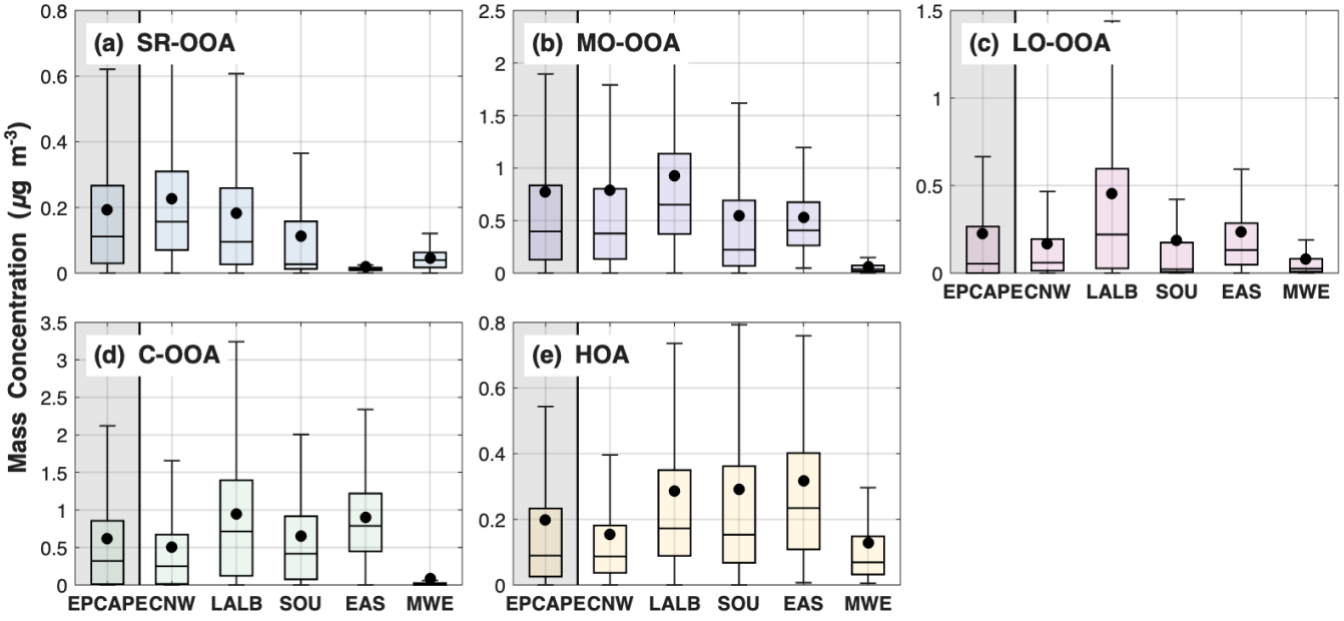

Figure 5. Box plots of 3-hour average mass concentrations (μg m^{-3}) of AMS NR (a) SR-OOA, (b) MO-OOA, (c) LO-OOA, (d) C-OOA, (e) HOA at Mt. Soledad, categorized by the five identified air mass origins (CNW, LALB, SOU, EAS, MWE). Mass concentrations exclude times with number concentrations exceeding 8000 cm^{-3}. The black dots represent the monthly means. The boxes indicate the interquartile range (IQR), with the middle line marking the median, the top edge representing the 75th percentile, and the bottom edge representing the 25th percentile. The whiskers extend to the maximum and minimum non-outlier values.

https://doi.org/10.5194/egusphere-2026-4695
Preprint. Discussion started: 24 August 2026

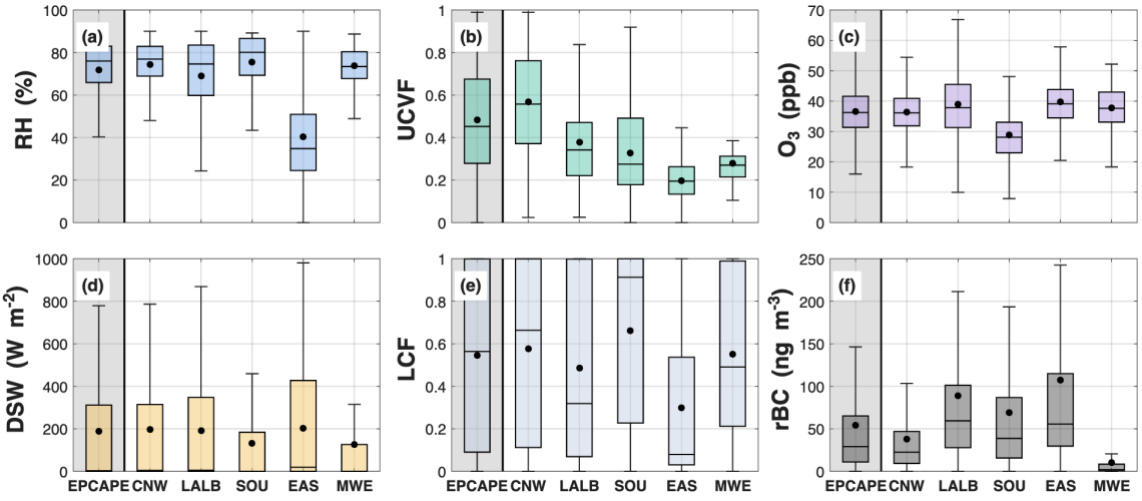

Figure 6: Box plots of 3-hour average values of RH, UCVF, O_3, DSW, LCF, and rBC at Mt. Soledad, categorized by the five identified air mass origins (CNW, LALB, SOU, EAS, MWE). O_3 and rBC exclude times with number concentrations exceeding 8000 cm^{-3}. The black dots represent the means. The boxes indicate the interquartile range (IQR), with the middle line marking the median, the top edge representing the 75th percentile, and the bottom edge representing the 25th percentile. The whiskers extend to the maximum and minimum non-outlier values.

https://doi.org/10.5194/egusphere-2026-4695
Preprint. Discussion started: 24 August 2026

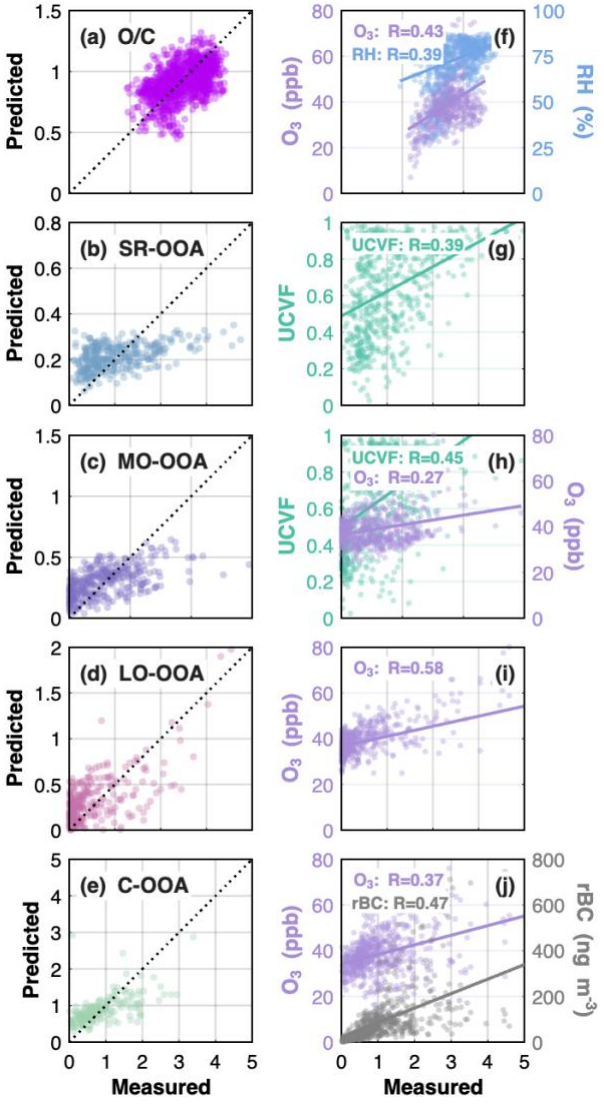

Figure 7: Measured versus predicted values for (a) O/C (unitless), (b) SR-OOA (μg m^{-3}), (c) MO-OOA (μg m^{-3}), (d) LO-OOA (μg m^{-3}), and (e) C-OOA (μg m^{-3}) from multilinear regression (MLR) models using O_3, RH, UCVF, rBC, and LCF as predictor variables. The left column shows measured versus predicted values for (a) O/C during the annual period, (b) SR-OOA during spring (Apr–Jun), (c) MO-OOA during spring, (d) LO-OOA during spring, and (e) C-OOA during fall (Oct–Dec). The right column shows relationships between the measured response variables and selected predictor variables averaged over 3 hours, including (f) O/C versus O_3 (during fall) and RH (during spring), (g) SR-OOA versus UCVF, (h) MO-OOA versus UCVF and O_3, (i) LO-OOA versus O_3, and (j) C-OOA versus O_3 and rBC. Solid lines represent linear regression fits, and the corresponding Pearson correlation coefficients (R) are shown in each panel. Colored scatter points correspond to the predictor variable indicated by the axis labels. The dotted line in the top row indicates the 1:1 relationship. The coefficient of determination (R^2) for each model is shown in Table 1.

https://doi.org/10.5194/egusphere-2026-4695
Preprint. Discussion started: 24 August 2026

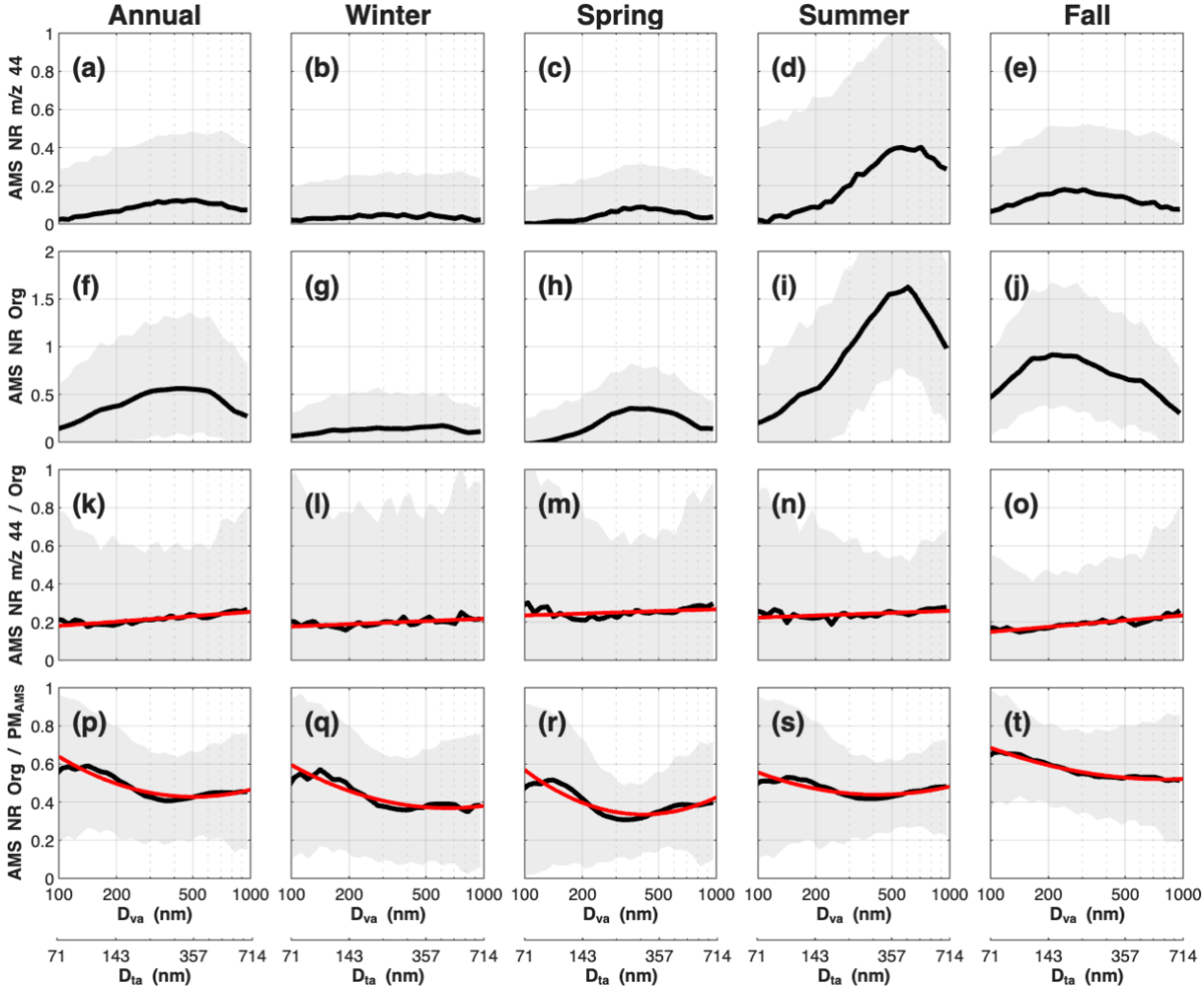

Figure 8: Mass distributions of AMS NR m/z 44 (µg m^{-3}; a–e), AMS NR organics (µg m^{-3}; f–j), the ratio of AMS NR m/z 44 to AMS NR organics (k–o), and the ratio of AMS NR organics to bulk AMS mass (PM_{AMS}; p–t) as a function of vacuum aerodynamic diameter (D_{va}) and the corresponding transmission aerodynamic diameter (D_{ta}), assuming a particle density of 1.4 g cm^{-3}. Columns correspond to annual conditions, winter, spring, summer, and fall from left to right. Solid black lines represent median values, and shaded regions indicate the interquartile range (25th–75th percentile). Red lines represent polynomial fits for the diameter range. All measurements exclude times with particle number concentrations exceeding 8000 cm^{-3}.

https://doi.org/10.5194/egusphere-2026-4695
Preprint. Discussion started: 24 August 2026

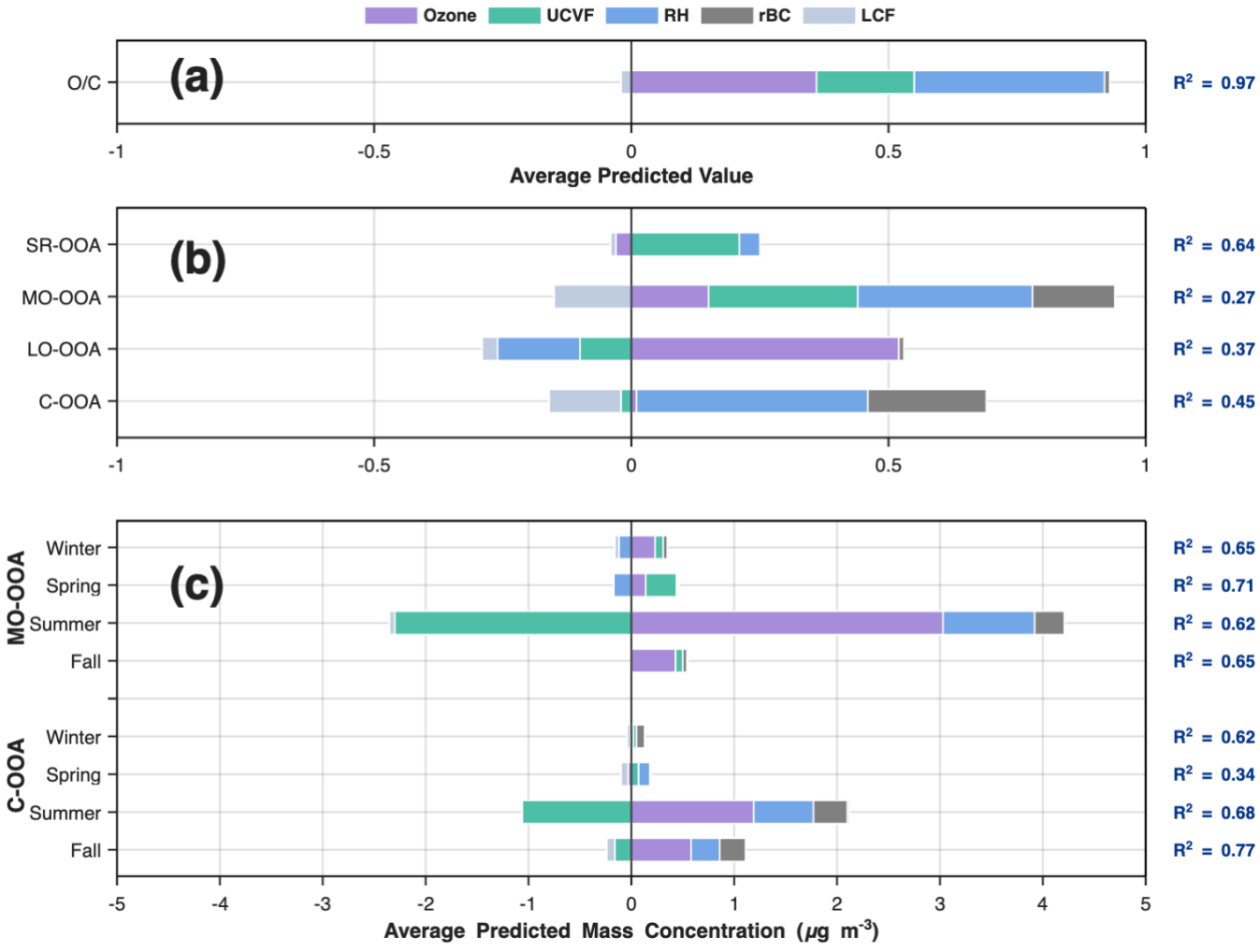

Figure 9: Relative contributions of O_3, UCVF, RH, rBC, and LCF to AMS NR organic O/C and PMF factor mass concentrations 1165 **derived from multilinear regression models. Contributions shown are calculated from normalized regression coefficients. Shown are annual models for (a) O/C, (b) SR-OOA, MO-OOA, LO-OOA, and C-OOA, and (c) seasonal models for MO-OOA and C-OOA, which exhibited stronger seasonal dependence than annual relationships. The coefficient of determination (R^2) for each model is shown on the right-hand side of each panel.**

https://doi.org/10.5194/egusphere-2026-4695
Preprint. Discussion started: 24 August 2026

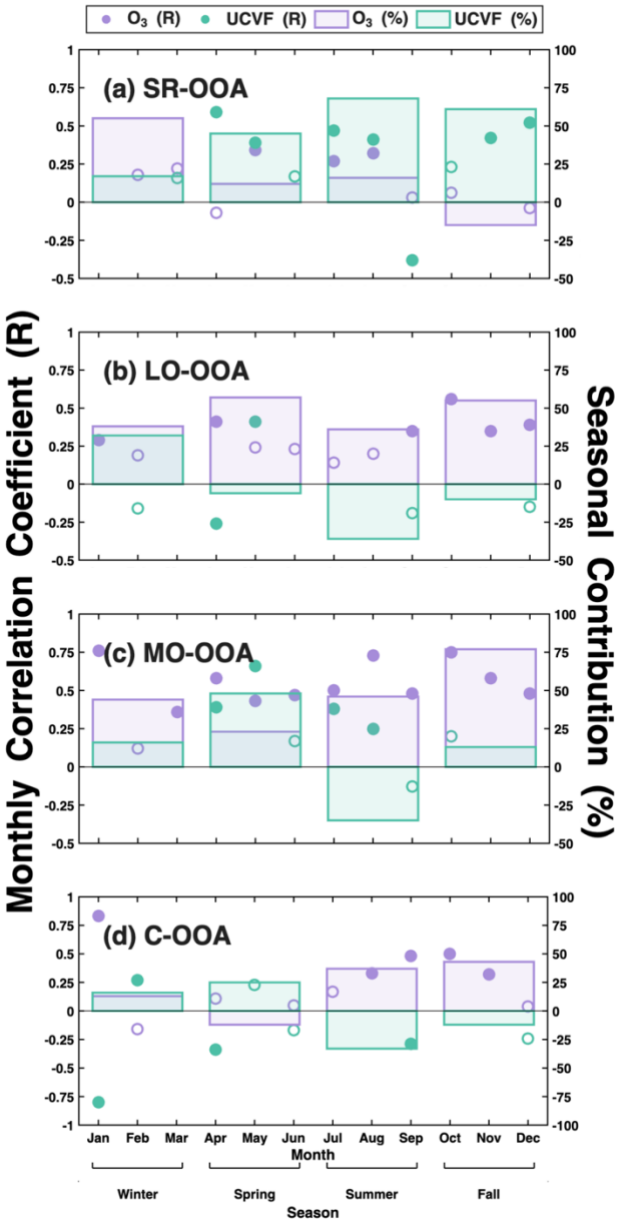

Figure 10: Comparison of monthly Pearson correlation coefficients (R; left axis) plotted as points and seasonal multiple linear regression (MLR) contributions (%; right axis) plotted as bars for (a) SR-OOA, (b) LO-OOA, (c) MO-OOA, and (d) C-OOA with ozone (O_3; purple) and upwind cloud vertical fraction (UCVF; teal). Monthly correlations are shown for January through December, while seasonal MLR contributions are shown for winter, spring, summer, and fall. Non-significant correlations ($p > 0.05$) were not plotted and points with correlations of $|R| < 0.25$ are not filled in.

https://doi.org/10.5194/egusphere-2026-4695
Preprint. Discussion started: 24 August 2026

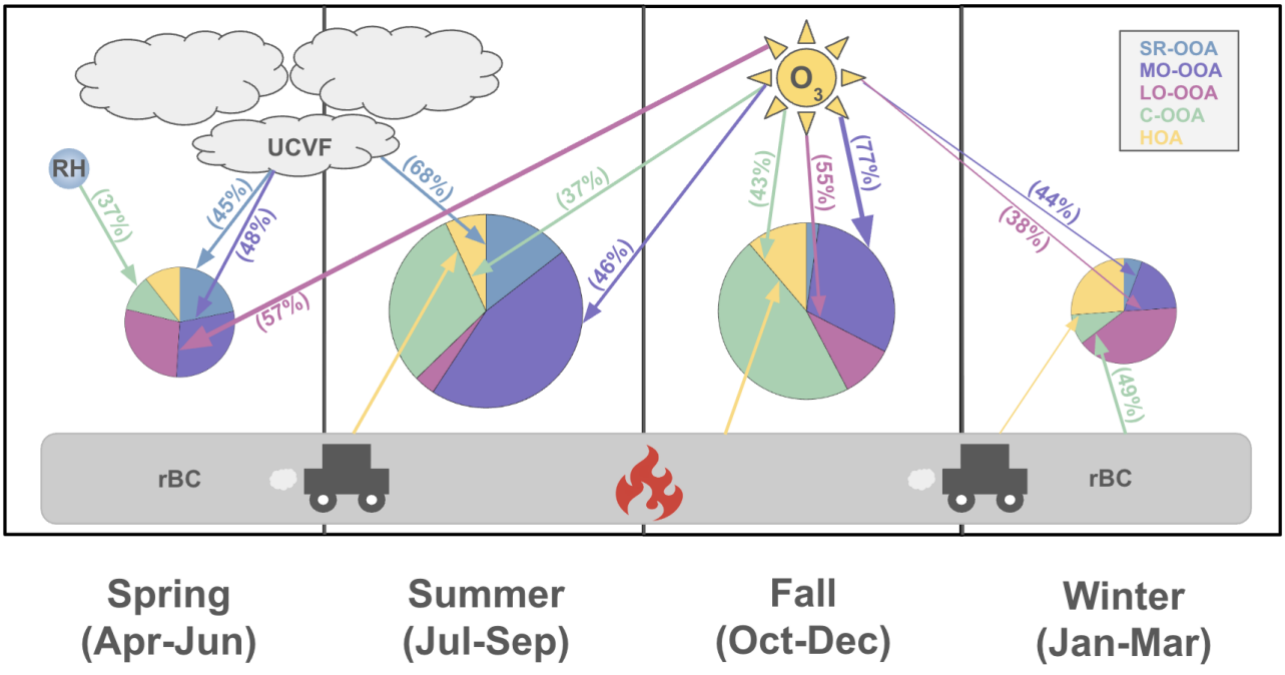

Figure 11: Schematic of the major PMF factors and the formation pathway contributing most strongly to their variability based on seasonal correlation coefficients for all PMF factors and multiple linear regression (MLR) analysis for OOA factors. Pie charts show the relative factor composition for each season, with pie size scaled by the seasonal average organic mass concentration. Arrows are shown for the four PMF factors with the largest seasonal mass fractions; arrow thickness is proportional to the corresponding seasonal correlation coefficient for all PMF factors, and seasonal MLR contributions (%) are indicated for the OOA factors. Photochemical reactions (O_3) are represented by the sun, in-cloud aqueous reactions (UCVF) are represented by the clouds, aerosol water aqueous reactions (RH) are represented by the hydrated particle, and mixed combustion (rBC) is represented by the cars and fire.